

國立台灣大學理學院地質科學所

碩士論文

Department of Geosciences

College of Science

National Taiwan University

Master Thesis

土衛八伊阿珀托斯赤道脊之彈性折彎模型模擬

**Elastic Flexure Model of Iapetus' Equatorial Ridge**

鄭懷傑

Whyjay Zheng

指導教授：葉永烜 博士，鄧屬予 博士

Advisor: Wing-Huen Ip Ph.D., Louis S. Teng Ph.D.

中華民國 102 年 1 月

January, 2013

國立台灣大學碩士學位論文  
口試委員會審定書

土衛八伊阿珀托斯赤道脊之彈性折彎模型模擬

Elastic Flexure Model of Iapetus' Equatorial Ridge

本論文係鄭懷傑君 (R99224106) 在國立臺灣大學地質科學研究所完成之碩士學位論文，於民國 101 年 12 月 27 日承下列考試委員審查通過及口試及格，特此證明

口試委員： 鄭懷傑 (簽名) 柳屬予 (簽名)

(指導教授) (指導教授)

鄭懷傑 柳屬予  
林盈暉

系主任、所長 鄧花華 (簽名)

## Acknowledgement

終於寫到了整本論文的最後一哩路。回首在台大地質系的點點滴滴，心中竟湧起無限的惆悵與感激。感激的是我何其幸運，在初探研究門扉時，便有許許多的貴人相助，順利完成此段學業；但惆悵的是或許以後有好一段時間，無法對著一樹的銀杏紅葉，抒發思古之幽情了。

在選擇接受碩士論文共同指導之後，才發現這的確不是件容易的事，但學生有幸的遇到兩位好老師：葉永烜老師總是不吝於給予學生學術上的指導，從題目的發想、研究的架構，一直到論文寫作上的協助，葉老師從不間斷的關心與建議，精進並強化了我在學術研究上的能力與熱情；而鄧屬予老師則扮演了心靈導師的角色，一旦學生在研究之路上遇到了各式各樣的阻礙，鄧老師總會仔細地聆聽，並且幫我精闢的分析，使學生獲得一生受用無窮的智慧。而論文能得以完稿，除了承蒙兩位指導老師全力協助外，尚得感謝願意擔任學生口試委員的台灣大學洪淑蕙老師、中央研究院趙丰老師與中央大學林殿順老師，提供使論文更臻完善的寶貴意見。Also very thanks Professor Bernd Giese, Professor Tilman Spohn and Professor Doris Breuer, who discussed with me and gave me many useful advices on my thesis work when vising Institute of Planetary Research (DLR) in Germany, 2012.

由於共同指導的緣故，得在中央大學與台灣大學兩邊跑。雖舟車勞頓，但也多虧於此，我才能結交來自不同領域的朋友，以及在研究室內一起打拼的夥伴。每次想起各位實在心懷感激：小麥跟塗翎總是能陪我打發在校車上的時間；宗富、晉銘、潮劭軒和泰豪是不認真 Meeting 時的好搭檔(!!)；小諭、白餅乾、陳徵(趕快加入吧!)還有 Alex 讓太陽系實驗室多了幾分活力；宇棋、LiChing、志仰、英同與省文前輩們使後生小輩受益良多；助理 Tracy 小姐每次都很貼心的處理所有行政上的職務；跟姊妹或小希的野外總是很放鬆地認真；而跟頌平或于倫的野外總是很認真地放鬆！與泰迪或賴瑞討論總是可以激發新的研究點子；品如學姊的家則是凝聚實驗室向心力的中心；阿刀、鎮源還有小黃學長們提供的撇步讓我總算順利畢業；芊學姊與宜伶學姊在學校行政流程上屢次不遺餘力的幫忙；也感謝其他太陽系實驗室的成員們、沉積與大地構造實驗室的成員們、台大地質 237 研究室的成員們、一起登山的隊員們，以及 B95 和 R99 志於從研究所畢業的夥伴們，因為有你們的包容與支持，才有這篇論文的誕生！回顧碩士生涯，或許在研究之外最令我印象深刻的就是地質調查導論二了，能夠擔任這門課的助教兩年半，實在是我的榮幸！謝謝鄧茂華老師與劉聰桂老師給我這麼多機會參與其中，更要深深的感謝每位老師、助教與學生的出力，共同完成了一段美好回憶。尤其是羅立、頌平和梅子，能夠與你們搭檔主持晚會，重拾大學時辦營隊的熱情與樂趣，真的非常開心！

最後，謝謝爸媽對於我的任何決定總是支持與鼓勵，雖然偶爾會好奇我什麼時候要畢業，但還是很放心的讓我放手去做；謝謝包包，就算是為了論文忽略了妳，凌晨兩點仍在趕工時，仍然會有貼心的按摩服務。因為有你們的陪伴，使我在人生的道路上不畏懼任何挑戰，滿懷著希望向前行。

## 摘要

土衛八伊阿珀托斯可能是太陽系中最具特異性之一顆衛星。在平均半徑約為 735 公里的星球上，有一列平均高度約 10 公里的山脊精準地落在其赤道上，這高聳的山脊甚至讓伊阿珀托斯的外型看起來像核桃般特異。此列山脊大概佔據了伊阿珀托斯超過 75% 的赤道總長，吾人即據此事實名之「赤道脊」。赤道脊在 2005 被卡西尼號探測器發現，但它的形成原理卻因缺少進一步的觀測證據，至今還在爭辯中；目前已經有數種不同的形成假說，並可以粗略地被分為內生性成因(板塊運動)或是外生性成因(環遺骸堆積物)。

另外，伊阿珀托斯的外型呈現扁橢球形，並可對應至一個自轉週期為 16 小時的液體球平衡外型。但伊阿珀托斯目前已受土星之潮汐鎖定，導致其自轉週期為 79 天。由於此衛星具有古老且隕石坑眾多的表面，潮汐鎖定事件和赤道脊形成的事件應也在衛星形成的早期( $> 4000$  Ma)即完成。如此一來，在赤道脊形成之時，伊阿珀托斯之表面應具有相當高之熱流值，使得地表易受到負重或板塊作用力的影響而彎曲。因此，只要利用此點，就可算出在赤道脊形成時，伊阿珀托斯表面之材料特性，再利用這些限制求出較可能之赤道脊起源。

本研究主要目的，即是利用彈性岩石圈理論，運用解析法及數值法，建構伊阿珀托斯赤道脊之折彎模型(Flexure Model)。赤道脊在此方法中被視為在伊阿珀托斯的硬外殼(彈性板)上完美之線狀負載，伊阿珀托斯的數值高程模型(DTM)不僅被作為建構赤道脊負載的量化依據，同時也顯露出赤道脊山腳有數公里深之凹陷證據。如此深的凹陷意味著彈性板厚度可能極小，如此一來伊阿珀托斯的硬外殼可以被視為平坦的單一薄板。另外從地質特徵觀之，伊阿珀托斯並無板塊作用(側向應力的存在)的證據。在解析式模型中，赤道脊被設定為一負載點，以上條件可令折彎與負載的關係簡化成一維線性常微分方程，輸入彈性板的厚度後，就可求得被折

彎之地表的情形。而在一維數值模型中，負載之函數則依赤道脊的外貌剖面建立，並使用有限差分法模擬折彎之地表。另外，因為隕石撞擊事件可能影響彈性板厚度，本研究也嘗試使用彈性板厚度隨位置變化之數值模型做為參考。

模擬結果顯示了與前人研究一致之訊息：超過 100 公里厚之彈性岩石圈將不會造成任何顯著的地表折彎。然而 DTM 高程提供的訊息(尤其是隆起處與赤道脊中心之距離)卻顯示其較有可能為 5-10 公里厚之彈性岩石圈作用下的結果。數值模擬結果也顯示了赤道脊區域的地型主要由隕石撞擊事件，以及薄彈性層折彎這兩因子所塑造。此一新結果雖與前人研究相異，但除了一部份疑似受隕石撞擊事件施以彈性層水平應力之區域外，對於 DTM 地形卻高度相符。如此薄的岩石圈，也說明了赤道脊形成時，伊阿破托斯內部具有高熱流通量( $\sim 18 \text{ mWm}^{-2}$ )。如此一來 16 小時週期之橢球外貌的形成，時間上應晚於赤道脊之形成。折彎模型中也顯示了赤道脊的原始高度可能較現今高出一倍，如此一來原始坡度就與環殘骸堆疊(外生性成因)後自然形成的堆積坡休止角較為相近而不矛盾。綜觀以上結果，由於並無明顯的證據支持內生性成因，因此較有可能之赤道脊起源仍屬外生性之環殘骸假說。

簡而言之，從地表地型資料與衛星熱史推論，伊阿珀托斯的彈性折彎模型顯示了赤道脊可能負載於一較薄(5-10 公里)之彈性板上，並且提供了更多關於伊阿珀托斯，這顆太陽系中有趣的衛星，其起源的更多線索。

#### 關鍵字：

伊阿珀托斯，彈性折彎模型，赤道脊，岩石圈，數值模擬

## Abstract

Iapetus may be the most peculiar satellite in the Solar System. This Saturnian moon has a mean radius of 735 km, but an averagely 10-kilometer-high mountain ridge lies precisely on its 75% equatorial circumference. The ridge is so high that Iapetus appears walnut shaped, and it is named “equatorial ridge” after this amazing truth. The ridge was discovered by the Cassini spacecraft in 2005, but the formation theory is still under debate because of the lack of observational data. Several hypotheses, which are roughly divided into endogenic (tectonic buckling) and exogenic (ring remnant) processes, are attributed to explain its origin.

Previous studies also noted that the shape of Iapetus is an oblate spheroid related to a hydrostatic spin period of 16 h, but Iapetus now is tidally synchronized with a 79-day period. Because the surface of Iapetus is old and heavily cratered, the formation of the ridge and the oblate spheroid had finished in the early stage of Iapetus ( $> 4000$  Ma). Thus, it’s plausible to assume that Iapetus had a high thermal flux when the equatorial ridge formed. The assumption leads to a result that the surface would bend when the applying load like the ridge exerted. Therefore, upon calculating the deflection of the surface, we could obtain some constraints for the thermal history of Iapetus, and the proper origin model of the equatorial ridge.

According to this idea, we attempted to construct analytical and numerical flexural models of the equatorial ridge by utilizing elastic lithosphere theory. The equatorial ridge is treated as a perfectly linear load on Iapetus’ hard shell (i.e. elastic layer of Iapetus). The Digital Terrain Model (DTM) data are inputted and transformed to a vertical load function, and also reveals that large deflection exists in some foothills area. This few-kilometre deflection implies a very thin elastic layer enough to regard it as a flat plate. Moreover, there are no tectonic signals on Iapetus, so the flat-Earth and one-plate condition could adapt to the flexure model. To obtain an analytical solution, the equatorial ridge is simplified to a central loading point. This can be rearranged into an explicit deflecting function in the 1-D coordinate system, so the deflection can be computed if the elastic thickness is given. In the numerical model, the point vertical force is replaced by a loading map.

The finite difference method is used to solve the ODE flexural function. Consider the elastic thickness may vary with different areas; we also set a variable-thickness program for the numerical modelling.

The modelling results illustrate that an over 100-km elastic layer would not cause any significant deflection; it coincides with the previous suggested. However, a deflecting curve with a range of 5-10 km elastic thickness well fits the terrain data, especially for the distance between a bulge and the ridge. Numerical solution also shows that there are 2 factors contributing the geomorphological changes: cratering and the flexure. Cratering created a deep hole and a thinner elastic layer. These new results seem controversial to the previous studies, but the modelled surface profile is highly consistent with numerical ridge DTM profile except the plateau regions which are suspected to be caused by cratering end load pressure. Such a thin shell implies that the ridge formed when the heat flux stayed high ( $\sim 18 \text{ mWm}^{-2}$ ). Therefore, the formation of the ridge probably happened before the despin (oblate shaping) event. The thin-layer flexure model also solves the problem of the angle of response because the ridge sank in the deflected surface, lowered the slope from the angle of response to the observed slope of the ridge. Since there is no evidence relating to endogenic processes, the exogenic origin is in favour.

In conclusion, the flexural model of Iapetus' equatorial ridge reveals the possibility of thinner (5-10 km) hard shell, fits the surface profile and thermal history, and supplies more clues to the origin of Iapetus, the interesting satellite in the Solar System.

**Key words:**

**Iapetus, Flexure model, Equatorial Ridge, Lithosphere, Numerical Model**

# Table of Contents

口試委員審定書	i
Acknowledgement	i
摘要	i
Abstract	iii
Table of Contents	v
List of Figures	vii
List of Tables	ix

## Chapter 1 Introduction 1

1.1 Saturn .....	1
1.1.1 The Ring System of Saturn	2
1.1.2 The Satellite System of Saturn	4
1.2 Iapetus.....	4
1.2.1 Observational History	5
1.2.2 Basic Physical Properties	7
1.2.3 Surface Features	9
1.3 Research Goals .....	10

## Chapter 2 Historical Researches 12

2.1 Geological Background of Iapetus .....	12
2.1.1 Shape and Rotation	12
2.1.2 Age	14
2.1.3 Inner Structure and Composition	15
2.1.4 Thermal History	16
2.1.5 Albedo Dichotomy	17
2.2 Geomorphological Data of Iapetus' Equatorial Ridge .....	19
2.3 The Origin Models and Flexural Implications of Iapetus' Equatorial Ridge...21	
2.3.1 Exogenic Models	23
2.3.2 Endogenic Models	25

<b>Chapter 3 Research Methods</b>	<b>28</b>
3.1 Introduction to the Flexure Model .....	28
3.2 Construction of the Flexure Model.....	29
3.2.1 Fundamental Formulae of the Flexure Model	30
3.2.2 2-D Flexure Equations of Elastic Plates	31
3.3 Analytical Flexure Model of the Equatorial Ridge .....	38
3.3.1 Material Properties of Iapetus	38
3.3.2 Basic Assumptions and Approximate Equations for the Ridge	41
3.3.3 Modeling Flow Chart	44
3.4 Numerical Flexure Model of the Equatorial Ridge .....	46
3.4.1 Differences between Analytic and Numerical	46
3.4.2 Modeling Flow Chart	47
3.5 Features against the previous studies of Iapetus' flexure model .....	49
<b>Chapter 4 Research Results</b>	<b>50</b>
4.1 Analytical Solution .....	50
4.1.1 Geomorphological Constraints of Elastic Thickness	56
4.2 Numerical Solution .....	57
4.2.1 Uniform Thickness	57
4.2.2 Variable Thickness	61
<b>Chapter 5 Discussion and Conclusion</b>	<b>63</b>
5.1 Interpretation of the Results .....	63
5.1.1 Ridge Area	63
5.1.2 Ultrahigh Bulge	63
5.1.3 Craters	64
5.2 Formation Model of the Equatorial Ridge .....	65
5.2.1 Possibility of a Thin Elastic Shell	65
5.2.2 Endogenic or Exogenic?	66
5.3 Chronology of Iapetus .....	67
5.4 Conclusion .....	68
<b>Chapter 6 References</b>	<b>69</b>

## List of Figures

Fig. 1-1 Ring System of Saturn .....	1
Fig. 1-2 Relative position of the major moons of Saturn .....	2
Fig. 1-3 Image of Iapetus .....	3
Fig. 1-4 Global Surface Image of Iapetus.....	6
Fig. 1-5 Equatorial Ridge on Iapetus.....	9
Fig. 2-1 Portion of image N1483174398.....	18
Fig. 2-2 Digital Terrain Model (DTM) of Iapetus .....	20
Fig. 2-3 Illustration for a ring-collapsing scenario .....	24
Fig. 3-1 A typical stress-strain curve.....	28
Fig. 3-2 An elastic plate pinned at its ends and bending under a load $q(x)$ .....	31
Fig. 3-3 A segment of the deflecting plate in Fig. 3-2 .....	32
Fig. 3-4 The small segment (with the length of $l$ ) of the plate.....	35
Fig. 3-5 The phase diagram of water.....	39
Fig. 3-6 Iapetus thermal radiation image .....	40
Fig. 3-7 Illustration of vertical forces on a deflected elastic plate .....	42
Fig. 3-8 Flow chart of the analytical flexural modeling .....	45
Fig. 3-9 Flow chart of the numerical flexural modeling .....	48
Fig. 4-1 The site of DTM profiles .....	50
Fig. 4-2 Analytical Flexural Modeling of Profile $r1$ .....	52
Fig. 4-5 Analytical Flexural Modeling of Profile $r4$ .....	53
Fig. 4-4 Analytical Flexural Modeling of Profile $r3$ .....	53
Fig. 4-3 Analytical Flexural Modeling of Profile $r2$ .....	53

Fig. 4-6 Analytical Flexural Modeling of Profile r5 .....	54
Fig. 4-7 Analytical Flexural Modeling of Profile r6 .....	54
Fig. 4-8 Analytical Flexural Modeling of Profile r7 .....	54
Fig. 4-9 Analytical Flexural Modeling of Profile r8 .....	55
Fig. 4-10 Analytical Flexural Modeling of Profile r10 .....	55
Fig. 4-11 Numerical Flexural Modeling of Profile r1.....	58
Fig. 4-12 Numerical Flexural Modeling of Profile r2.....	58
Fig. 4-13 Numerical Flexural Modeling of Profile r3 .....	58
Fig. 4-14 Numerical Flexural Modeling of Profile r4 .....	59
Fig. 4-15 Numerical Flexural Modeling of Profile r5 .....	59
Fig. 4-16 Numerical Flexural Modeling of Profile r6 .....	59
Fig. 4-17 Numerical Flexural Modeling of Profile r7 .....	60
Fig. 4-18 Numerical Flexural Modeling of Profile r8 .....	60
Fig. 4-19 Numerical Flexural Modeling of Profile r10.....	60
Fig. 4-20 Modeling of Profile r9 with Various Lithospheric Elastic Thickness.....	61

## List of Tables

Table 1 Basic Parameters of Iapetus.....	8
Table 2 Origin Models of Iapetus' Equatorial Ridge.....	22
Table 3 Parameters of The Equatorial Ridge for Every Profile.....	51



# Chapter 1 Introduction

## 1.1 Saturn

Saturn is the second largest planet in the Solar System. It is located on an average distance of 9.58 AU away from the Sun. This giant planet belongs to a member of Jovian Planets, and is composed of mainly gaseous matter (96.3% hydrogen and 3.25% helium) and a small amount of solid matter (ice and silicate rocks) as its inner core (Willians, 2012). The high ratio of gaseous matter lowers the average density of Saturn with only  $687 \text{ kg/m}^3$ , which is much less than Jupiter, Uranus and Neptune (Willians, 2012). There are many interesting properties of Saturn's atmosphere and inner structure; however, the most intriguing one may be its ring and satellite system.

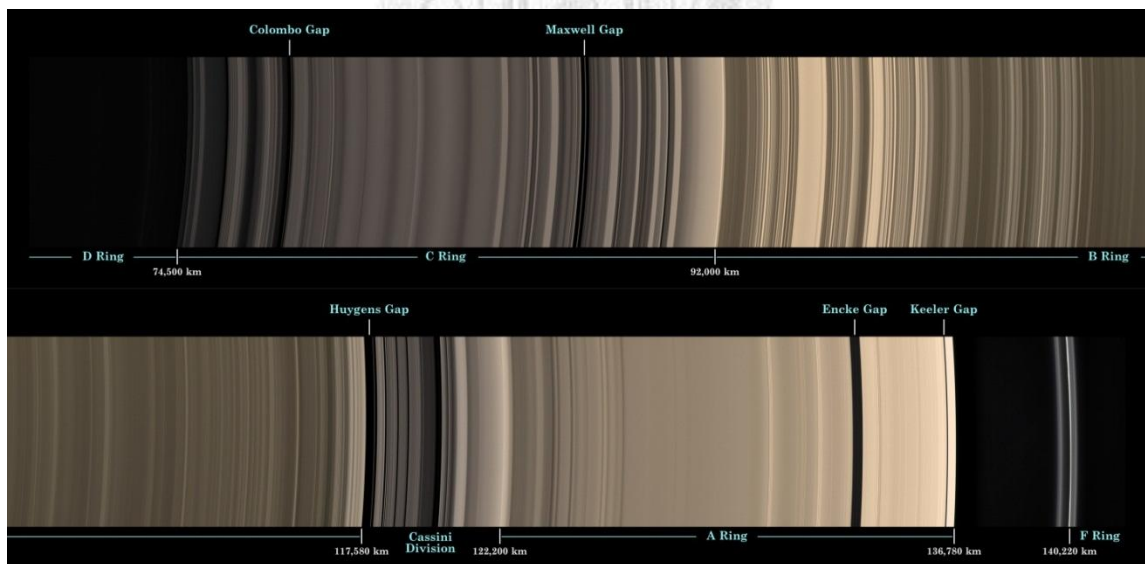


**Fig. 1-1 Ring System of Saturn.** PIA08389, Courtesy of NASA. Horizontal axis stands for the distance away from the center of Saturn.

### 1.1.1 The Ring System of Saturn

Saturn's rings which consist of dust particles are multi-layered. The whole ring system can be divided into several layers by the ring gaps, whose particles are sparser than ring layers (e.g. Huygens Gap in Fig. 1-1). The particles stuffed in the rings are sized from 1 centimeter to ten meters, and constructed a vertically thin layer (Zebker *et al.*, 1985). According to IAU nomenclature, D ring occupies the most inner part of the ring system, and the next is C, B, A, F ring and so on. Fig. 1-1 displays the relative position of the ring system. There are also some ring layers beyond the F ring; for instance, Phoebe Ring spans from ~4 million kilometers to over 13 million kilometers away from the center of Saturn (Verbiscer *et al.*, 2009). Due to the improvement of observation technology, new rings outside the F ring are continuously discovered. The outer edge of Saturn's rings still remains ambiguous

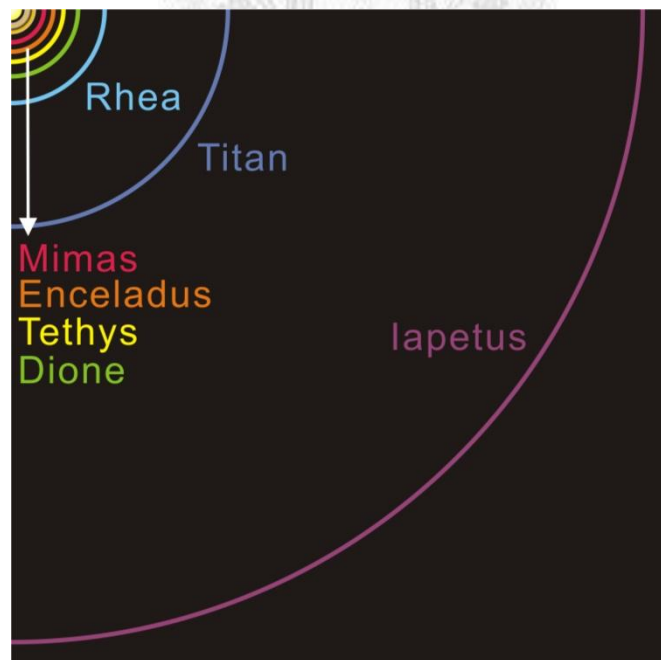


**Fig. 1-2 Relative position of the major moons of Saturn.**

since the reflected light of ring edge is too dim to detect.

The origin of Saturn's rings is also ambiguous. Previous studies suggested that the age of the rings may be old, but the precise age remains unknown (Kerr, 2008). The rings were interpreted to be the wrecks of a satellite. After a huge impact event, the satellite was scattered into particles. For those particles which were in the Roche limit of Saturn, they remained scattered due to the affection of tidal force.

Rings may interact with nearby satellites. These satellites, often called "shepherd moons", help the rings to stabilize the ring system. For example, two moons Prometheus and Pandora maintain the shape of the F ring and prevent any gravitational interruption.

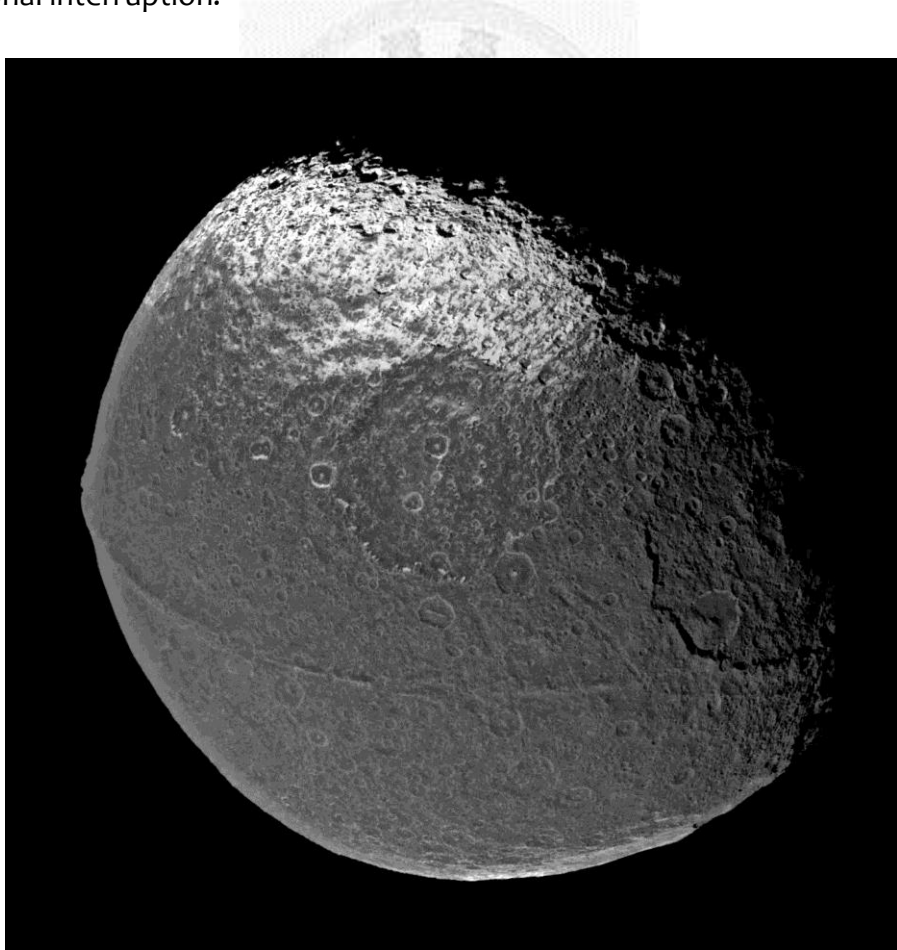


**Fig. 1-3 Image of Iapetus.** PIA06166, courtesy of NASA.

### 1.1.2 The Satellite System of Saturn

Saturn has numerous satellites with a high variety of features. Most of them are too small to form spheroids. Only 7 moons are ball-shaped: (arranged with the distance from Saturn) Mimas, Enceladus, Tethys, Dione, Rhea, Titan and Iapetus. Fig. 1-2 also shows the distance between each major satellites and Saturn.

The 7 moons have their own geologic features. Mimas is the smallest known gravitational rounded astronomical body in the Solar System. It's highly tidal-stretched, so it appears egg-shaped. Enceladus is geologically active due to cryovolcanism. Water may exist under its surface ice layer. Tethys has a large crater Odysseus and a large canyon Ithaca Chasma. These 2 features may have relationship in the early age of Tethys. Some ice cliffs exist on the surface of Dione; this perhaps implies the geologic activity similar to Enceladus. Recent researches suggested that Rhea may have its own ring system (Jones *et al.*, 2008; Schenk *et al.*, 2011). It would become the first satellite which has a ring around itself. Titan is the largest moon of Saturn; it is also the only satellite covered with thick atmosphere. Therefore, Titan is regarded as a hotspot of astrobiology which may help us to understand the early stage of life. Finally, Iapetus is the topic of this study. The next section will discuss more details of Iapetus.

## 1.2 Iapetus

Iapetus is the third largest satellite of Saturn, also the 11th largest satellite in the Solar System (Yeomans, 2012). Fig. 1-3 taken by Cassini-ISS (Imaging Science Subsystem) shows the outline of this satellite. Although its mean radius is only 734.3

km (Thomas, 2010), peculiar geomorphological features make Iapetus become a focus of planetary science. This section will simply introduce the basic knowledge of Iapetus, including observations and important features.

### 1.2.1 Observational History

Iapetus was first discovered by Giovanni Domenico Cassini in October 25<sup>th</sup>, 1671. After several decades of observation, he found that if Iapetus appears on the western side of Saturn, it is always brighter than viewing it on the eastern side of Saturn (van Helden, 1984). Hence, Cassini surmised that Iapetus must be tidally locked by Saturn, and that it has a brightness difference between the two sides of Iapetus. In other words, the bright side faces the Earth when Iapetus is on the western side, and the dark side emerges when Iapetus is on the eastern side. His conjecture was confirmed by Cassini-Huygens spacecraft 2 centuries later. The dark side of Iapetus nowadays is named Cassini Regio in honor of his excellent contribution.

After Cassini's observation, humans didn't know much more about Iapetus until the arrival of Cassini-Huygens spacecraft in 2007. Cassini-Huygens is a spacecraft mission conducted by NASA (National Aeronautics and Space Administration), ESA (European Space Agency) and ASI (Italian Space Agency) (Munsell, 2012). Its main goal is to study the science of Saturn and its natural satellites. Cassini-Huygens includes a Saturn orbiter called Cassini and an atmospheric probe, called Huygens, for its moon Titan. It launched on October 15<sup>th</sup>, 1997 and reached Saturn on July 2004. Huygens probe separated from Cassini orbiter five months later, and successfully entered Titan's atmosphere on January 14<sup>th</sup>, 2005. Huygens performed

excellently since it finally landed on Titan's surface and returned data to the Earth. It's also a first probe that landed on the outer Solar System. On the other hand, Cassini orbiter investigated many aspects of Saturn during different flybys. On September 10<sup>th</sup>, 2007, Cassini had its first and only flyby of Saturn's distant moon, Iapetus, just 1640 km above its surface (Munsell, 2012). Many images and data were taken (Fig. 1-3), including instrumental observations of Cassini's Visible and Infrared Mapping Spectrometer (VIMS), ISS, Composite Infrared Spectrometer (CIRS), Ultraviolet Imaging Spectrograph (UVIS) and RADAR detection (Jet Propulsion Laboratory, 2007). The observational details will be discussed in the next chapter. After this flyby, no other flyby events or plans are suggested until 2012.

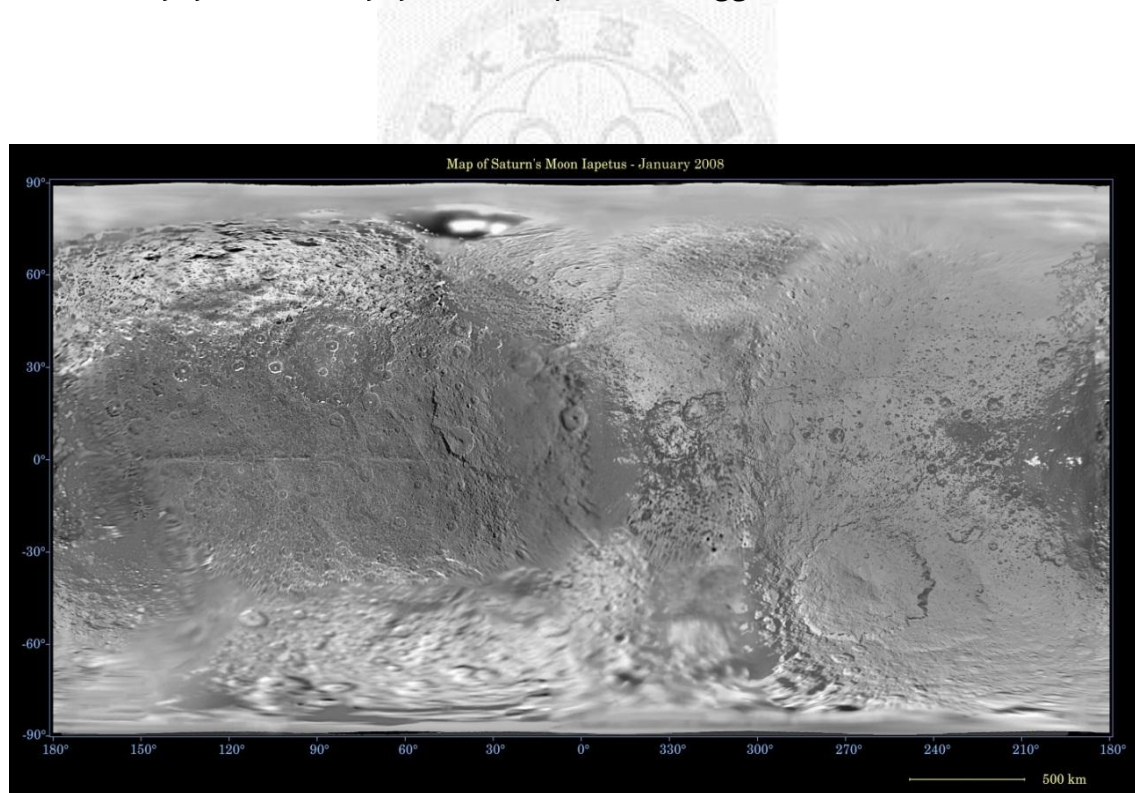


**Fig. 1-4 Global Surface Image of Iapetus.** PIA08406. Courtesy of NASA.

### 1.2.2 Basic Physical Properties

Most detailed physical properties of Iapetus were measured by Cassini spacecraft. Compared to the other satellites of Saturn, Iapetus has some abnormal parameters. First, from Fig. 1-2, Iapetus has the largest orbital semi-major axis and inclination among all major satellites of Saturn (Castillo-Rogez *et al.*, 2007). Although there are dozens of small satellites like Phoebe outside Iapetus, they are too small to form spheroids. Iapetus is big enough to maintain its spheroidal shape, but it is highly flattened. The lengths of Iapetus' 3 axial radii are listed in Table 1. C-axis is set to the polar radius, which is only 95% of the equatorial radius. Iapetus' mean density listed in Table 1 is only  $1.088 \text{ g/cm}^3$ . It's also the smallest mean density in all Saturn's major satellites. That implies Iapetus may be mainly composed of water ice (near  $0.9 \text{ g/cm}^3$ ) or have a porous inner structure, and silicate materials may occupy 20% or less of Iapetus' total weight (Castillo-Rogez *et al.*, 2007).

Another unique property of Iapetus is its albedo variability. The global topographic map of Iapetus (Fig. 1-4) was made from mosaic images taken by Cassini ISS. Iapetus is highly synchronized with Saturn, and the terrain of the leading side (left side in Fig. 1-4, often called Cassini Regio) shows darker than Iapetus' trailing side. The albedo is 0.05 for the leading side and is 0.5 for the trailing side (Willians, 2012). The boundary of albedo dichotomy is also obvious. This phenomenon is exclusive in the Solar System, and becomes a highlight of Solar System science. The hypotheses of the formation of albedo dichotomy will be mentioned in the next chapter.

**Table 1 Basic Parameters of Iapetus**

Orbital Properties	
Semi-major Axis (m)	$3.561 \times 10^9$ <sup>*</sup>
Eccentricity	0.0283 <sup>*</sup>
Inclination (°)	14.72 <sup>*</sup>
Orbital Period (days)	79.33 <sup>*</sup>
Physical Properties	
Mean Radius (km)	$734.3 \pm 2.8$ <sup>†</sup>
Oblate Semi-major Axis (km)	745.7, 745.7, 712.1 <sup>†</sup>
Mean Density (kg/m <sup>3</sup> )	1088 $\pm$ 13 <sup>†</sup>
Rotation Period (days)	79.32 <sup>‡</sup>
Equatorial Surface Gravity (m/s <sup>2</sup> )	0.220-0.223 <sup>‡</sup>
Albedo	0.05-0.5 <sup>*</sup>
Mass (kg)	$1.806 \times 10^{21}$ <sup>§</sup>

<sup>\*</sup>: Willians, 2012.

<sup>†</sup>: Thomas, 2010.

<sup>‡</sup>: Roatsch *et al.*, 2009.

<sup>§</sup>: Jacobson *et al.*, 2006.

### 1.2.3 Surface Features

The surface of Iapetus is highly cratered. Several huge craters can be seen on Fig. 1-4. The diameter of the largest crater is 580 km, equal to ~78% of Iapetus' mean radius (USGS Astrogeology, 2009). The fact of cratering implies 2 points at least: 1) Iapetus presently has no significant geologic processes; and 2) All the surface features on Iapetus must be old except some mass wasting events, which will be discussed in the next chapter.

Iapetus also has the most peculiar surface feature that was uncovered by Cassini orbiter. Denk *et al.* (2000) have first detected it in Voyager data, but no further description until 2007 Cassini flyby. Just as previously mentioned, Iapetus has an equatorial bulge that outlines an oblate spheroid of Iapetus; but stranger than the bulge is its equatorial ridge. Equatorial ridge is a huge structure on Iapetus, and can be seen on the global view of this satellite (Fig. 1-2 and 1-4). The closer view of

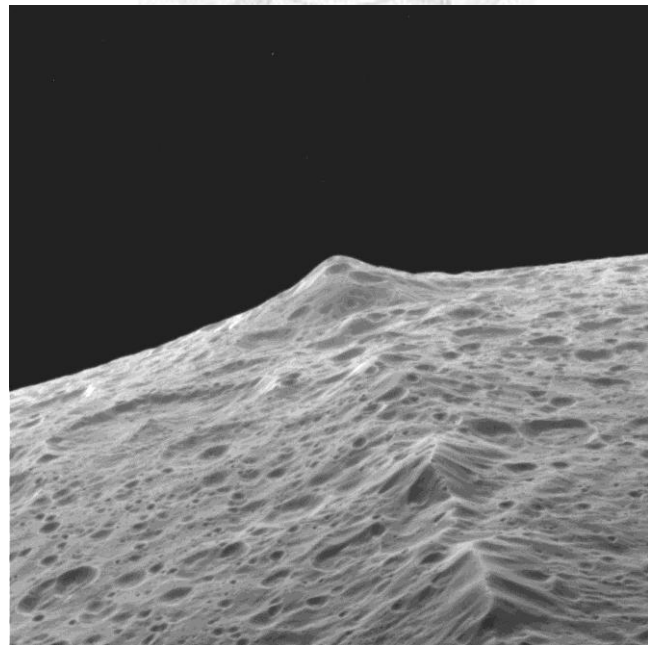


**Fig. 1-5 Equatorial Ridge on Iapetus.** PIA08404. Courtesy of NASA.

the equatorial ridge is showed by Fig. 1-5 taken by Cassini orbiter. This mountain lies precisely on the equator and runs over 75% of the circumference (Singer & McKinnon, 2011). Cassini observations (Porco *et al.*, 2005) reported that the equatorial ridge typically has a triangular cross-section with a base of 200 km and a height of up to 20 km. Some parts of equatorial ridge have devastated by cratering, but the well-preserved section of the ridge spans over 1600 km, that is, over one third of the circumference. The existence of the ridge do not relate to the albedo dichotomy since the ridge is continuous on the dichotomy boundary. The flanks of the ridge are steep with over 20 degrees in some areas (e.g., Giese, Denk *et al.*, 2008). The estimated volume of this mountain is  $\sim 3 \times 10^6$  km<sup>3</sup> ( $\sim 0.1\%$  of total volume of Iapetus), excluding any mountain roots. The ridge is also an old structure since the surface of the ridge is dominated by craters, like other areas on Iapetus. This mountain is also the main topic of this study.

### 1.3 Research Goals

After the exploration of Cassini spacecraft, we could get more information about these 2 unique features (the albedo dichotomy and the equatorial ridge). There is one intriguing question among all the research topics related to Iapetus: how did the equatorial ridge form? Is there any distinctive process on the formation of the ridge? Until 2012, many studies on Iapetus tried to suggest models explaining the formation of the equatorial ridge. These models include despinning (Castillo-Rogez *et al.*, 2007), collapse of Iapetus' ring system (Ip, 2006), contraction theory (Sandwell & Schubert, 2010), convection theory (Czechowski & Leliwa-Kopystyński, 2008), magmatic intrusion (Melosh & Nimmo, 2009), large

impact event (Dombard *et al.*, 2012). It is still under debate about which model is more possible. Therefore, this study will change the sight toward the ridge to another aspect. We first examine the possible restricted physical conditions the ridge, and the last select the more possible model for interpreting the formation of the ridge.

Flexure model is a powerful tool for analyzing the layered structure of the lithosphere on the Earth. In order to construct the inner structure of Iapetus (especially in the ridge area), this study utilizes the flexure model as a major tool. Although there is no gravitational anomaly and laser altimeter data, Giese, Denk *et al.* (2008) have transferred the Cassini ISS images into the Digital Terrain Model (DTM). They overlapped different images, which photographed the same area in Iapetus. Based on the program calculation, they gathered the more detailed DTM data of Cassini Regio on Iapetus. Most previous studies pointed out that there isn't any flexure signal caused by the loading of the equatorial ridge (Dombard *et al.*, 2012; Giese, Denk *et al.*, 2008), but in this study shows the high possibility of a thin-shell flexure signal in the foothills of the ridge. This study attempts to construct both analytical and numerical models of flexure model, and deducts the possible boundary conditions of the ridge. These conditions may correlate with some origin models. Finally, these conditions would reveal a likelihood of the ridge formation.

## Chapter 2 Historical Researches

### 2.1 Geological Background of Iapetus

So far, most data and images of Iapetus are observed by the 2007 flyby of Cassini orbiter. Several models have been mentioned to construct the geologic inferences of Iapetus. These models are usually classified into different topics: shape and rotation, inner structure, age, albedo dichotomy of exosphere, and equatorial ridge. All topics will be described next except the origin models of the equatorial ridge, which will be discussed in section 2.3.

#### 2.1.1 Shape and Rotation

Iapetus is a satellite that has a shape of oblate spheroid (746×746×712 km, from Table 1), and its rotation period is tidally synchronized with a 79-day orbiting period (Porco *et al.*, 2005). The highly flattened shape of Iapetus is possibly caused by rotational flattening since the amount of a-c axis difference is large enough to ignore the effect of crater modifying. But 79-day rotation period is too slow to form an oblate spheroid. Consider an equilibrium of gravitational field and centrifugal acceleration due to rotation, the flattening coefficient,  $f$ , is given by

$$f = \frac{R_e - R_p}{R} = \frac{5}{4} \frac{\omega^2 R^3}{GM} \quad (2-1)$$

where  $R$  is the mean radius of the satellite,  $R_e$  and  $R_p$  stand for the equatorial and polar radius (a and c axis) of the satellite,  $\omega$  and  $M$  are the angular velocity and the

mass of the satellite, and  $G$  is the gravitational constant. The parameters listed in Table 1 are adopted to calculate the status of hydrostatic equilibrium for the current rotation period. If Iapetus is homogeneous, the estimated a-c difference ( $R_e - R_p$ ) is only 2.53 m. It doesn't match with the current shape of Iapetus. Thus, Iapetus doesn't have an equilibrated shape nowadays, and must possess a despinning history.

In the meantime, the hydrostatic equilibrium of the shape of Iapetus yields a predicted period of 16.5 h (from Eq. 2-1). If there was a silicate core inside Iapetus, it would be required a spin period of 15.2 h to form this oblate spheroid (Castillo-Rogez *et al.*, 2007). So, Iapetus has a fossil shape that formed in the early age of Iapetus. When the rock strength of Iapetus increased due to cooling, Iapetus fixed its outline.

Another issue is that how long did Iapetus despin to the synchronization? In fact, all satellites of Saturn, except Hyperion, are tidally locked by Saturn. However, synchronous spin on Iapetus is less possible than the other Saturnian satellites since Iapetus has both large mass and semi-major axis (Peale, 1986). Ip (2006) and Matson *et al.* (2009) also suggested that Iapetus need much time that possibly more than the age of the Solar System, except that the interior are mostly molten. To describe more precisely, we uses the following formula to calculate the damping time of tidal locking (Gladman *et al.*, 1996; Peale, 1977):

$$t_{lock} \approx \frac{\omega_i a^6 I Q}{3 G M_p^2 k_2 R^5} \quad (2-2)$$

where  $\omega_i$  is the initial angular velocity of the satellite ( $1.06 \times 10^{-4}$  radian/sec),  $a$  is the

semi-major axis of the satellite,  $I$  is the moment of inertia ( $\approx 0.4MR^2$ ) of the satellite,  $Q$  is the dissipation function of the satellite,  $M_p$  is the mass of the planet (which is Saturn in this case,  $5.6846 \times 10^{26}$  kg (Willians, 2012)),  $k_2$  is the tidal Love number of the satellite. In general,

$$k_2 \approx \frac{1.5}{1 + \frac{19\mu}{2\rho g R}} \quad (2-3)$$

where  $\mu$  is the rigidity of the satellite (usually  $4 \times 10^9$  Nm $^{-2}$  for icy satellites),  $\rho$  is the mean density of the satellite,  $g$  is the surface gravity of the satellite. Set a generic  $Q$  of solid bodies = 100, Eq. 2-2 and 2-3 yield a tidal-locking time of 277 My. Since  $Q$  has a high uncertainty which ranged from 10-500 for solid icy satellites (Dobrovolskis *et al.*, 1997), Iapetus may have a tidal dissipation timescale of 28-1400 My. Based on the calculation, we can conclude that it requires the existence of partial melting on the early stage of Iapetus inner core to synchronize its spin, or Iapetus may have spent long time (roughly 100-1000 My) to do so.

### 2.1.2 Age

Porco *et al.* (2005) reported that Cassini ISS images showed the heavily cratered surface of Cassini Regio. The whole surface except the equatorial ridge area is controlled by the cratering, with over 3 large ones whose diameters are larger than 350 km. The study of size distribution of craters (Kirchoff & Schenk, 2010) suggests that the terrain age of both dark side and bright side are the same. The high density of craters on Iapetus implies that Iapetus may be geologically old.

A quantitative value of the age of Iapetus is predicted by Castillo-Rogez *et al.* (2009, 2007). They set a model considering the shape, despinning and the thermal history of Iapetus, and the best-fit age value is between  $\sim 3.4$ - $5.4$  Myr after the formation of calcium-aluminum inclusions (CAIs). The age of CAIs was measured by Amelin *et al.* (2002), who proposed an age of  $4567.2 \pm 0.6$  Myr from Pb-Pb dating method. Thus the age of Iapetus is 4563.8 to 4561.8 My. Since all the surface features on Iapetus appear old, they might form on the early stage of Iapetus. The crater frequencies analyzing result (Neukum *et al.*, 2005) also implied an over 4-billion-year surface on Iapetus. Based on lunar crater studies, the age of the surface of Iapetus is probably close to 4400-4500 Myr.

### 2.1.3 Inner Structure and Composition

As previously mentioned, Iapetus has 2 possible internal structures: 1) Iapetus has a large portion of low-density materials; 2) Iapetus has a porous inner core. If Iapetus is composed of low-density materials, then water ice is the most likely matter since ice has a low density ( $0.9 \text{ g/cm}^3$ ) similar to the density of Iapetus. In the model proposed by Leliwa-Kopystyhski *et al.* (1994), Iapetus is set to have an icy mantle of 418-km thickness and a silicate inner core (whose density is  $3.361 \text{ g/cm}^3$ ) of 328-km radius. But the radius of the inner core decreases when mantle is mixed with ammonia ( $\text{NH}_3$ ) and methane ( $\text{CH}_4$ ), which are the bulk compounds in the Jovian planets. In the other hand, Owen *et al.* (2001) analyzed the infrared spectrum of 0.3-3.8  $\mu\text{m}$  to get the information of the surface composition of Iapetus. They found that the surface of Cassini Regio is deposited by the mixed matters of water ice, amorphous carbon, and nitrogen-rich compounds. After Cassini orbiter's

observation, Buratti *et al.* (2005) obtained the VIMS data for Iapetus, and concluded that the bright side is ice-rich so that it appears the high albedo; and that the detection of carbon dioxide ( $\text{CO}_2$ ) in the dark side implies the removal of the regolith. Cruikshank *et al.* (2010) even noted that the  $\text{CO}_2$  on Iapetus is native, enclathrated in water ice, and then released due to the exposure of the solar wind. Therefore, an acceptable model is that the bulk composition of Iapetus is  $\text{H}_2\text{O}$ , and that there are compounds which are rich in carbon, nitrogen inside the water ice.

A porous inner core may exist, but is less possible due to a lack of gravitational data. Sandwell and Schubert (2010) used this hypothesis to construct a model of the formation of the equatorial ridge, which will be discussed later.

#### 2.1.4 Thermal History

Thermal history is the key to the chronology of Iapetus. If the tidal-dissipating time is relatively short, sufficient heat is needed for the partial melting of the inner core. Furthermore, the fossil 16-h shape implies a core which generated large amount of heat but lost it quickly. Castillo-Rogez *et al.* (2007) noted that  $^{26}\text{Al}$  could play a significant role on the early stage of Iapetus.  $^{26}\text{Al}$  is one of short-lived radioactive isotopes (SLRI), which include the common radioactive isotopes with the half-life of under several million years.  $^{26}\text{Al}$  is also abundant in CAIs, but quickly decay to  $^{26}\text{Mg}$  with a half-life of 0.716-0.73 Myr (Kita *et al.*, 2005). Castillo-Rogez *et al.* (2009) also pointed out that the abundance of  $^{26}\text{Al}$  dominated the age, the porosity changes, and the shape evolution. Their modeling result shows a possible  $^{26}\text{Al}$ -rich scene: after Iapetus formed (with the age mentioned in section 2.1.2), the heating from radioactive nuclides lowered the strength of the material of Iapetus, shaped

an oblate spheroid. When Iapetus synchronized its spin within 200-1000 Myr, no more  $^{26}\text{Al}$  radioactive heat was generated so that the satellite was cooling down, remaining a 16-h fossil shape.

### 2.1.5 Albedo Dichotomy

Iapetus' albedo dichotomy can be easily recognized in Fig. 1.4. The Cassini Regio (dark side) distributes over low to mid-latitude regions, and is constrained in 0-210 degrees of longitude. Squyres and Sagan (1983) first noted that there is a one-magnitude difference of albedo between the dark side and the bright side. The VIMS survey mentioned in 2.1.3 offered a possible composition of these 2 sides (Buratti *et al.*, 2005; Cruikshank *et al.*, 2010): The bulk composition of the bright side is water ice, however the matters on the dark side mixed with several compounds including  $\text{H}_2\text{O}$ ,  $\text{CO}_2$ , and N-rich organic compounds which are often called tholins. Because we observed that  $\text{CO}_2$  emitted from ice clathrates, it is accepted that the dark side is regolith-depleted; in other words, the deep rock of Iapetus is exposed to the surface because of the removal of the weathering soil.

Dozens of hypotheses were proposed to explain the origin of the dichotomy. For instances, Owen *et al.* (2001) interpreted the dark side as debris deposits, which were originated from Titan. On the other hand, Marchi *et al.* (2002) regarded the dichotomy as a result of Iapetus-Hyperion collision event. Wilson and Sagan (1996) also suggested that there is a removal of ice on the dark side, and then the dark matters were exposed; the trigger of the removal of ice is numerous impact events from interplanetary dust particles. Most of these hypotheses are related to exogenic procedures. In the recent study, a new model is illustrated by Spencer and

Denk (2010), who plausibly explained the albedo dichotomy as a global thermal migration of water ice. In this model, a slight albedo difference is given in the beginning. Since Iapetus has an unusual synchronous spin, the day temperature is high enough to sublimate water ice. If there is a slight albedo dichotomy on Iapetus, water ice in the dark side will be sublimated during daytime. The gaseous H<sub>2</sub>O will migrate and deposit in the bright side, and then increase the albedo of the bright side. This positive feedback enlarges the difference of the two sides, and finally depletes the water ice in the dark side. The process costs 2400 Myr to form the nowadays condition of Iapetus. Because Iapetus need  $\sim 10^9$  years to be synchronized, the albedo dichotomy may be a “new” structure on the Iapetus, or still in development.

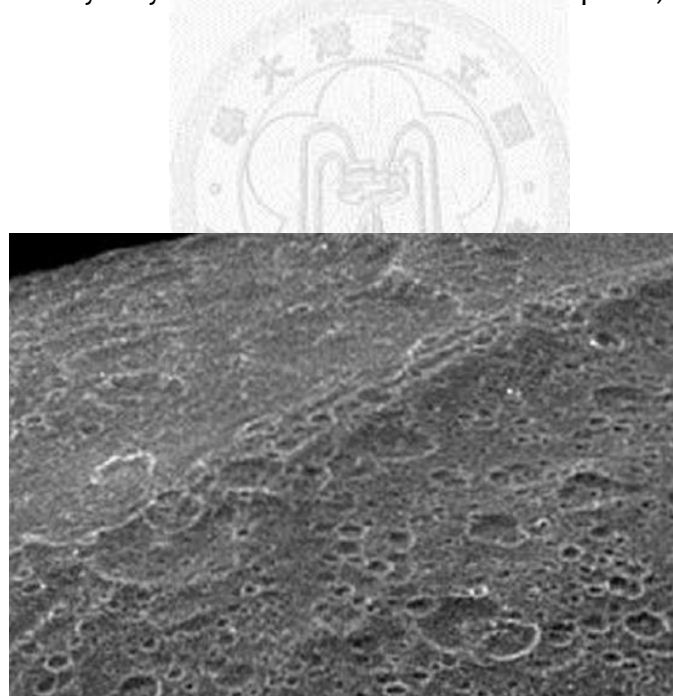


**Fig. 2-1** Portion of image N1483174398. From Porco *et al.* (2005).

## 2.2 Geomorphological Data of Iapetus' Equatorial Ridge

The earliest mosaic images of Iapetus are published by Porco *et al.* (2005). Fig. 2-1 is one of the images of the peculiar equatorial ridge. The ridge in Fig. 2-1 shows 2 features: 1) several parallel linear structures aligning the ridge; and 2) heavily cratered surface with some parts which is devastated (the lower left corner of the ridge in Fig. 2-1).

To obtain more detailed morphological data of Iapetus, Thomas *et al.* (2007) employed the limb coordinates and stereogrammetric control points which were measured by the Cassini ISS. They treated Iapetus as an oblate spheroid with  $747.4 \times 747.4 \times 712.4$  km. And the next, the limb area (especially in the equatorial bulge) of each image is located and measured. Finally, Thomas *et al.* gathered 31 limb profiles of the equatorial bulge area. However, Giese, Denk *et al.* (2008) pointed out that the limb profile may be over-estimating on the height of the equatorial ridge. They used another way to construct the Digital Terrain Model (DTM) data of Iapetus.

Their simple idea is to superimpose multiple images which have control points and picture at the same area of Iapetus. The shadowed area that is caused by the highlands of Iapetus varies when the position of the orbiter changes, so the height of the surface is obtained by superimposing images taken by Cassini ISS from different places. Giese, Denk *et al.* utilized their method to icy satellites including Enceladus (Giese, Wagner *et al.*, 2008), Phoebe (Giese *et al.*, 2006), and of course Iapetus. Fig. 2-2 displays the calculated DTM data of leading side (dark side). (Giese, Denk *et al.* also noted that the DTM height of the ridge is 10-20 km, which a width of 100-200 km and an average slope of 4-10 degrees. The DTM data shows a lower

ridge than previous suggestion by Thomas *et al.* (2007), but the precision of the surface profile is enhanced. For example, the A-A' profile in Fig. 2-2 cuts through a crater, the ridge, a depression area and a plateau area; this profile distinguishes them respectively. The resolution of DTM data is kilometer-scale, but the small structure of such this scale may be ignored when modeling; that is, DTM data is useful on large-scale structures like big craters or the ridge, but it is not so precise for the small structures.

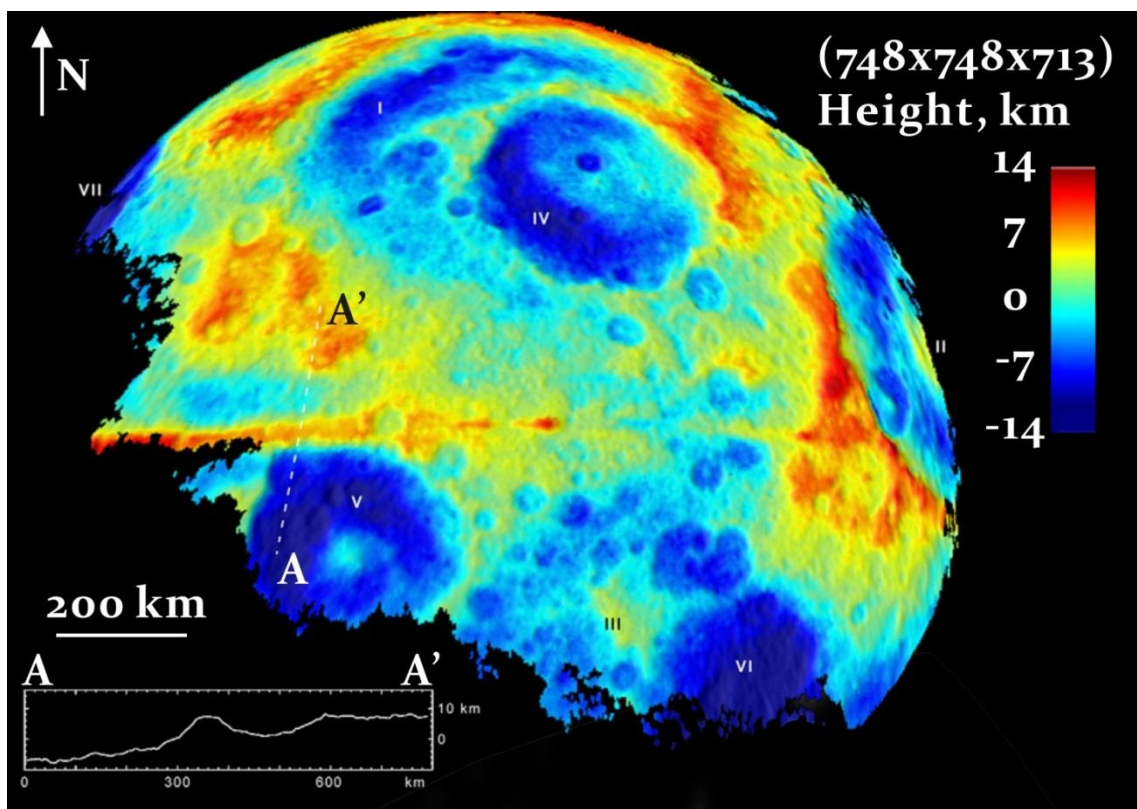


**Fig. 2-2 Digital Terrain Model (DTM) of Iapetus.** Reference shape is a  $748 \times 748 \times 713$  oblate spheroid. A-A' profile cuts through the depression area, the ridge and crater No. 5. Modified from Giese, Denk *et al.* (2008).

## 2.3 The Origin Models and Flexural Implications of Iapetus' Equatorial Ridge

The equatorial ridge is also an old structure since the crater density is similar to the other areas of Iapetus. If we accept the crater-frequency dating proposed by Neukum *et al.* (2005), the ridge has remained its shape for over 4 billion years. Although there is a fossil 16-h equatorial bulge, the ridge seems to be excluded from the bulge and superimposes on it. Obviously, the ridge was not formed simply by despinning, and the other scene is needed to explain the origin of the ridge.

Until 2012, the ridge has been interpreted into several different origins, which can be divided into two main classes: endogenic model and exogenic model. Due to the lack of *in situ* survey, it is still under debate that which one is more correct. The brief descriptions of these models are listed in Table 2 for the detailed discussion in the next section.

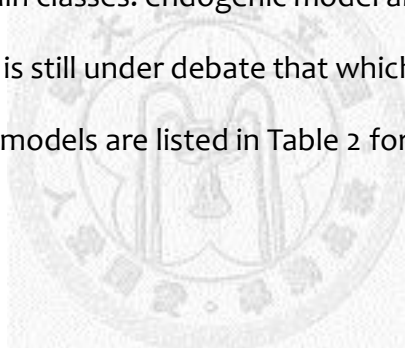


**Table 2 Origin Models of Iapetus' Equatorial Ridge**

Author(s) and year	Model Class	Description
Ip (2006)	Exogenic	The collapse of the ring system, which originated during Iapetus' formation
Castillo-Rogez <i>et al.</i> (2007); Porco <i>et al.</i> (2005)	Endogenic	Tectonic activity triggered by the despinning
Dombard <i>et al.</i> (2012); Levison <i>et al.</i> (2011)	Exogenic	The collapse of the ring system, which originated from an impact event
Giese, Denk, <i>et al.</i> (2008)	Endogenic	Endogenic tectonic unwarping (fold)
Czechowski and Leliwa-Kopystyński (2008)	Endogenic	The rising point in the two-cell convection
Melosh and Nimmo (2009)	Endogenic	Igneous dike intruded in a thin lithosphere
Sandwell and Schubert (2010)	Endogenic	Lithosphere was applied by the contraction stress, which originated from a porous core

### 2.3.1 Exogenic Models

Porco *et al.* (2005) first noted that the equatorial ridge may originate from the same process that formed the equatorial bulge. Castillo-Rogez *et al.* (2007) expanded this idea and developed a model to evaluate the possibility of a despinning scenario. In this model, the ridge is interpreted to what was buckled when Iapetus started to slow down its rotation from a high initial spin rate. Set the thickness of lithosphere is 15 km, and then a 5-h initial spin rate is adequate to redistribute enough amount of material ( $\sim 3.5 \times 10^6 \text{ km}^3$ ) that reaches the volume of the ridge ( $\sim 3 \times 10^6 \text{ km}^3$ ). Although there's a high uncertainty affected by the lithospheric thickness, the initial spin rate is so close to the 3.8-h Roche limit that it hardly maintain a shape of oblate spheroid.

Therefore, the despinning scenario is doubtful. Ip (2006) computed that the despinning has not likely finished for limited age of the Solar System, just as discussed in section 2.1.1. He also suggested a new exogenic model that describes the ridge as deposits of a ring system remnant. Just like Saturn or the other gaseous planets, satellites may have their ring system during the formation stage. Iapetus' dust particles in the ring system might collide and drag with each other, making a dissipation of energy. This condition resulted in the decay of the ring orbit, and that numerous particles impacted on the equator of Iapetus, accumulating an equatorial ridge. Similar phenomenon was recently discovered on another Saturian satellite, Rhea, which has a completed equatorial linear trace that was soon interpreted as a ring remnant, although the total mass is much lesser than the equatorial ridge (Schenk *et al.*, 2011). Ip also proved that the possible volume of the Iapetus ring is sufficient to accrete the nowadays equatorial ridge. Fig. 2-3 simply describes the

process he proposed, and it makes sense that why the ridge lies precisely on the equator.

Based on the previous idea, the exogenic model has been developed by Levison *et al.* (2011) and Dombard *et al.* (2012). These two studies suggested that an ancient giant impact created Iapetus' ring system. Dombard *et al.* noted that if both Iapetus and its ring system have formed from the Saturian subnebula, it would have not been explained why the equatorial ridge was only found in Iapetus. Alternatively, they proposed the model that the ring formation may be posterior to the formation of Iapetus due to a unique catastrophic incident on Iapetus. Levison *et al.* (2011)

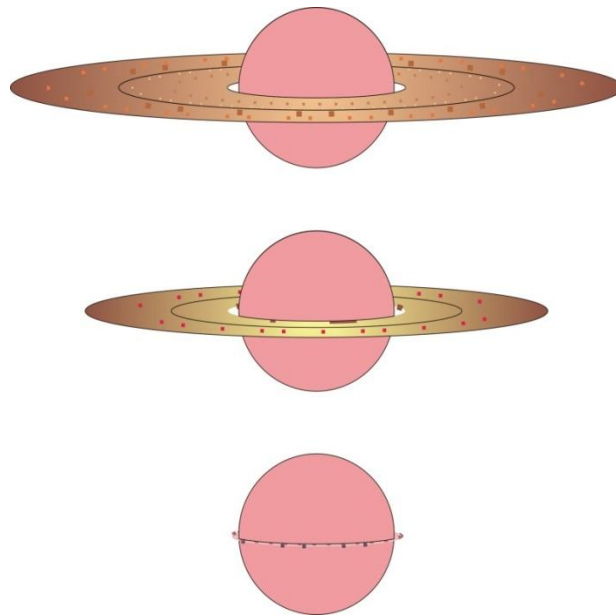


**Fig. 2-3 Illustration for a ring-collapsing scenario**, modified from Ip (2006). Top: Iapetus owned its ring system. Middle: The ring system gradually decayed its orbital radius due to the tidal dissipation. Bottom: The remnant of the ring deposited on the equator of Iapetus, building the ridge. Dombard *et al.* (2012) and Levison *et al.* (2011) used similar process to explain the transformation from an impact event to the equatorial ridge.

presented a scenario that the impact debris built the ring straightly; while Dombard *et al.* (2012) proposed that the impact may form a subsatellite first, and then this subsatellite decayed its orbit, eventually entering the Roche limit of Iapetus, torn into pieces, building the ring indirectly. After the ring formed, the accumulation scene is similar to Fig. 2-3.

### 2.3.2 Endogenic Models

Some researchers preferred endogenic models which need some special structural conditions. Giese, Denk *et al.* (2008) first pointed out that the ring remnant deposits should build a steep hill and a sharp peak, whose angle of response is up to 30-40 degrees. However, the average slope of the equatorial ridge is only 8-15 degrees (Giese, Denk *et al.*, 2008), and the topography of the peak revealed by their DTM model is really flat. Therefore, they argued that the ridge may not be formed by an exogenic process, but an ancient tectonic activity. Steep slopes and top-flatted peaks can be simply attributed to tectonic upwarping. They also figured out that there are some depressions aligned with the equatorial ridge; these depressions may stand for the flexural signals.

Next, Sandwell and Schubert (2010) expanded their study for the equatorial ridge. They suggested an innovative model describing a porous inner core (where porosity is over 10%) and a solid outer shell in Iapetus' early stage. When the inner core was heated and reached about 200K, the core began shrinking and lost the support force to the outer shell. Then the shell must deform its shape to match the volume with the inner core. The equatorial ridge is such a product of this buckling process. If the ridge was buckled, the flexure model can be used to construct a

relation between the thickness of the outer shell and the buckling type. This model in the spheroid case is suggested by the following formula (Beuthe, 2008; Sandwell & Schubert, 2010):

$$W_l = q_0 \left[ \frac{\eta D}{R^4} \frac{l(l+1)[l(l+1)-2][l(l+1)-2]}{[l(l+1)-1+v]} - \frac{F}{R^2} \frac{[l(l+1)-2][l(l+1)-2]}{[l(l+1)-1+v]} + \frac{Eh}{R^2} \frac{[l(l+1)-2]}{[l(l+1)-1+v]} + \Delta\rho g \right]^{-1} \quad (2-4)$$

$$\eta = \frac{12R^2}{12R^2+h^2} \quad (2-5)$$

where  $W$  is the vertical deformation (flexure value) in terms of Legendre polynomials,  $q_0$  is the vertical load,  $D$  is flexural rigidity which will be mentioned in Chapter 3,  $R$  is the radius of the satellite,  $E$  and  $v$  are Young's modulus and Poisson ratio of the material,  $F$  is the end load,  $h$  is the thickness of the lithospheric outer shell,  $\Delta\rho$  is the change of density between the core and the space (where the value is equal to  $\rho$ ), and  $g$  is the surface gravity of the satellite. The  $l$  value in Eq. 2-4 is a factor of the frequency domain, and  $l=2\pi kR$  approximately. The denominator of Eq. 2-4 explains a composition of flexural frequencies. The lesser the amount of the denominator is, the larger the portion of the flexure is. Sandwell & Schubert found that if the buckling forms the type of the ridge whose harmonic degree ( $=2\pi R/\lambda = kR$ ) is 2, the thickness of the lithospheric shell should exceed 120 km. This model is plausible since it does not need an ultra-high initial spin rate of  $5 \cdot h$  and a strictly constrained thermal history. Nevertheless, it can't explain the depressions aligned with the ridge because thick shell didn't cause obvious regional depressions.

Another different endogenic model was proposed by Czechowski and Leliwa-Kopystyński (2008). Their model assumed a convective flow inside Iapetus. The properties of the material and the amount of the heat flow both affect the convective patterns. If parameters are chosen properly, Iapetus will show a pattern of 2-cell convection. In the 2-cell convection, the heat material flow upwells in the equator, and subducts in the polar region. In other words, the role of the ridge is like the mid-ocean ridges on the Earth. The disadvantages of this model is that we don't find any structures implying subduction near the pole of Iapetus; moreover, it's difficult to build such a high ridge only pushed by the thermal buoyancy (Dombard & Cheng, 2008).

Besides, there is also a creative model suggested by Melosh and Nimmo (2009). They regarded the ridge as an intrusive dike which occurred where the shell is the thinnest and hottest. It's similar to the scene of convection model, but they noted that the model doesn't need any convective patterns. When tidal dissipation generated heat on Iapetus, the heat soon concentrated in the Iapetus' equator, thinning the lithosphere. Thus, heat flow upwelled in the equator, generated a ridge.

## Chapter 3 Research Methods

### 3.1 Introduction to the Flexure Model

Flexural model originates from the studies of lithosphere and plate tectonics on the Earth. This theory was first developed in the 1970s for the rising of the theory of plate tectonics. 3 main geomorphological observations imply the lithosphere may obey the elastic deformation mechanism: 1) post-glacial rebound; 2) the gravity anomaly of the seamount chains; 3) the buckling of the convergent plate boundary. Walcott (1970) proposed a concept that the upper lithosphere must deform elastically because the temperature and the pressure are low here. Although Walcott noted that the proper description of the lithospheric deformation is viscoelasticity in large time scale, the model only considering elasticity is worth to be a reference model since it is simple and has minor bias.

Material behavior is mostly constrained by stress, temperature and pressure. Fig. 3-1 shows the typical stress-strain curve of the material, and this curve is divided

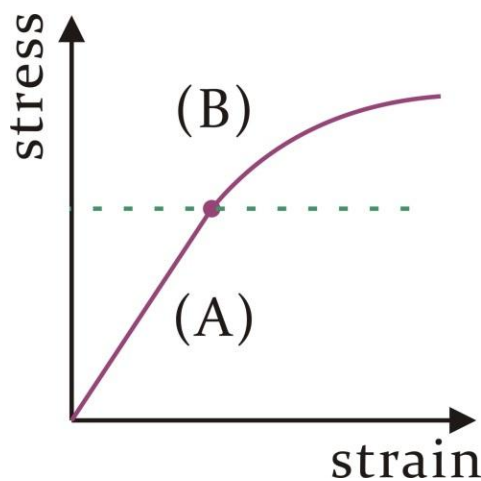


Fig. 3-1 A typical stress-strain curve.

into (A) and (B) regions. In (A) region, stress is proportional to the strain, and the material obeys elastic deformation (Hook's law); In (B) region, stress is beyond the elastic limit (the boundary stress of (A) and (B) region), the material deforms plastically or is fractured (brittle deformation). The elastic limit which controls the type of deformation is affected by both temperature and pressure. If temperature and pressure are low, material shows mainly elasticity.

In the theory of plate tectonics, the plate must be applied an end load (by the tectonic force) and a vertical load (by the surface deposits). If we ignore the brittle deformations such as faults and fractures, the whole plate can be treated as an elastic material. Thus, the geomorphological features and the gravity anomaly are the outcome of the bending plate, and then the thickness of this plate can be found out by solving formulae listed in the next section. This thickness is also called the "elastic thickness of lithosphere". Studies showed that the elastic thickness of oceanic lithosphere is ranged from 2-50 km, and that the elastic thickness of continental lithosphere is scattered with 5-100 km (Watts *et al.*, 1982). The elastic thickness cannot represent the thickness of whole lithosphere since the lower lithosphere may deform plastically, but it is highly bound with geothermal gradient or thermal conductivity. For example, the elastic thickness increases when the age of sea-floor increases because the older sea-floor has the smaller geothermal gradient, enlarging the thickness affected by elastic deformation (Watts *et al.*, 1982).

### 3.2 Construction of the Flexure Model

The flexure model is built on the elastic plate theory, which has been well

studied for mechanical engineers for several tens of years. The structure of the flexure model in this paper mainly refers to the books, separately written by Watts (2001) and Turcotte and Schubert (2002). It will be simply described.

### 3.2.1 Fundamental Formulae of the Flexure Model

It's generally assumed that an elastic plate can be described by Hook's law; that is, the stresses originating from the bent plate are proportional to the strain. Thus, we will first introduce basic relationships of the stress and strain. Consider a 3-D stressed material, and define that the scalar components of stress vectors ( $\sigma$ ) and strain vectors ( $\varepsilon$ ) exerting on the  $x$ ,  $y$ ,  $z$  axis are  $\sigma_1$ ,  $\sigma_2$ ,  $\sigma_3$ , and  $\varepsilon_1$ ,  $\varepsilon_2$ ,  $\varepsilon_3$  respectively. The relationship between stress and strain is described by the following 2 parameters: 1) Young's modulus ( $E$ ), which represents the ratio of the axial strain to the axial stress in a laterally unrestricted material; 2) Poisson's ratio ( $\nu$ ), which represents the ratio of lateral extension to longitudinal extension in a laterally unrestricted material exerted by the axial stress. With these 2 parameters, the connection between stress and strain can be easily written as

$$\varepsilon_1 = \frac{1}{E} \sigma_1 - \frac{\nu}{E} \sigma_2 - \frac{\nu}{E} \sigma_3 \quad (3-1)$$

$$\varepsilon_2 = \frac{-\nu}{E} \sigma_1 + \frac{1}{E} \sigma_2 - \frac{\nu}{E} \sigma_3 \quad (3-2)$$

$$\varepsilon_3 = \frac{-\nu}{E} \sigma_1 - \frac{\nu}{E} \sigma_2 + \frac{1}{E} \sigma_3 \quad (3-3)$$

Given distinctive stress and strain conditions, these stress and strain components can be solved by Eq. 3-1 to 3-3. A common assumption used in geology

is uniaxial strain, that is, when sediments were buried, it would be laterally constrained. Thus,  $\varepsilon_2=\varepsilon_3=0$ , and Eq. 3-1 to 3-3 will be simplified to

$$\sigma_2 = \sigma_3 = \frac{\nu}{1-\nu} \sigma_1 \quad (3-4)$$

$$\sigma_1 = \frac{(1-\nu)E\varepsilon_1}{(1+\nu)(1-2\nu)} \quad (3-5)$$

In the next section, we will discuss the conditions on elastic plates, and illustrate the flexure equations from the above formulae.

### 3.2.2 2-D Flexure Equations of Elastic Plates

Consider an elastic plate shown in Fig. 3-2. The plate has a width (x-direction) of  $L$  and a thickness (y-direction) of  $h$ , and is infinitely long in the z-direction. A line force  $q(x)$  in unit of z direction ( $\text{Nm}^{-2}$ ) applies on the plate and bends it. Note that  $q(x)$  will not change if z coordination varies. We define the deflection function  $w(x)$  to describe the vertical displacement of the plate. For example, a downward

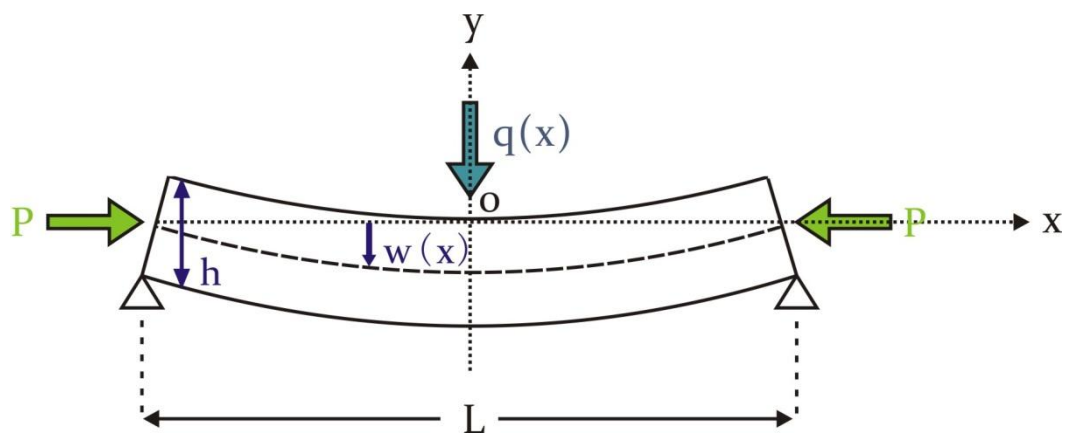
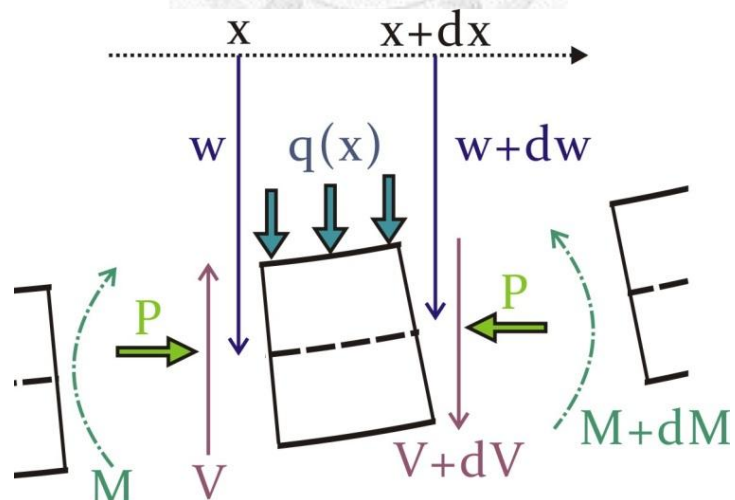


Fig. 3-2 An elastic plate pinned at its ends and bending under a load  $q(x)$ .

displacement  $w(x)$  shown in Fig. 3-2 is considered negative. The plate is pinned at its ends, that is,  $w$  is always equal to 0 on the edge of the plate. To simplify calculation, we assume that the plate is thin compare to its width,  $h \ll L$ , and so is the deflection function,  $w \ll L$ . Therefore, the linear elastic equations could adapt to this case. This 2-D bending case is often called cylindrical bending since the plate is a beam taken from a cylindrical shape of the bending.

Fig. 3-3 shows a segment of the deflecting plate. The deflection is the outcome of the equilibrium with all the forces and torques in Fig. 3-3. The small segment has a coordination of  $x$  and a width of  $dx$ . The downward load  $q(x)$  is exerted on the segment, so the combined downward force between  $x$  and  $x + dx$  is  $q(x) dx$  ( $\text{Nm}^{-1}$ ). Another force in the vertical direction is the shear force, which is  $V$  at location  $x$  and  $V + dV$  at location  $x + dx$ . Obviously,  $dV$  is also a downward force because the segment is sheared by the adjacent segments and the right side has a stronger upward shear force. Thus, a force balance in the vertical direction can be



**Fig. 3-3 A segment of the deflecting plate in Fig. 3-2, with applied forces and torques. Modified from Turcotte and Schubert (2002).**

constructed by equilibrating these 2 forces:

$$q(x)dx + dV = 0 \quad (3-6)$$

On the other hand, there are 3 types of torque acting on this segment. One is the net bending moment, which is the integrated moment on the cross section of the segment. The moment originates from the normal stresses of the cross section  $\sigma_{xx}$ , also known as fiber stresses. The bending moment is  $M$  at  $x$  and is  $M + dM$  at  $x + dx$ . Based on the same reason of the direction of  $dV$ ,  $dM$  is considered counterclockwise. The other torque is attributed by the horizontal force  $P$  ( $\text{Nm}^{-1}$ , per unit length in the  $z$  direction). The values of  $P$  in the both side of the segment are the same, but the  $y$  coordination is different. The deflection is  $w$  at  $x$  and is  $w + dw$  at  $x + dx$ , so the vertical distance of acting points of the two sides is  $dw$ . It results in a counterclockwise torque of  $-P dw$ . The minus sign is needed since  $dw$  is obviously negative, just mentioned before. The third one is the torque created by the shear force. The moment arm of the shear force is the width of this segment  $dx$ , so the torque is  $V dx$  clockwise. (The torque produced by  $dV$  can be ignored since  $dV$  and  $dx$  are both infinitesimal.) A torque balance of all the above yields

$$dM - Pdw = Vdx \quad (3-7)$$

Differentiate Eq. 3-7 twice, ant it gives

$$\frac{d^2M}{dx^2} = \frac{dV}{dx} + P \frac{d^2w}{dx^2} \quad (3-8)$$

Substituting Eq. 3-6 into Eq. 3-8 obtains

$$\frac{d^2M}{dx^2} = -q + P \frac{d^2w}{dx^2} \quad (3-9)$$

The next step will be to find an expression of  $M$  in a function of deflection.  $M$  is the integration of the fiber (longitudinal) stress  $\sigma_{xx}$ ; to find  $\sigma_{xx}$ , we construct a relationship between fiber stress and longitudinal strain  $\varepsilon_{xx}$ . Fig. 3-4 shows a small section of the bending plate with an infinitesimal length  $l$ .  $R$  and  $\varphi$  in this figure are the radius and the angle of curvature of this section respectively. The length change  $\Delta l$  is proportional to the distance ( $y$  component) from the midplane ( $y = 0$ ). Thus, the longitudinal strain is obtained by the following equation:

$$\varepsilon_{xx} = -\frac{dl}{l} = -\frac{y\phi}{l} = -\frac{y}{l} \frac{l}{R} = -\frac{y}{R} \quad (3-10)$$

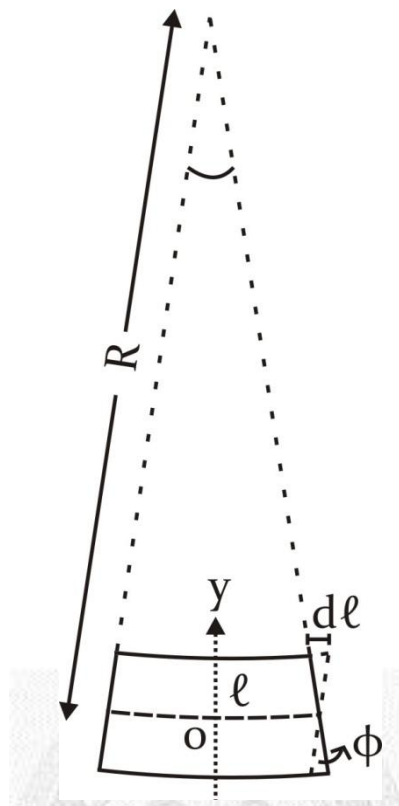


**Fig. 3-4 The small segment (with the length of  $\ell$ ) of the plate.** Strain

varies with  $y$  value. Modified from Turcotte and Schubert (2002).



Note that  $\varepsilon_{xx}$  is negative when  $y$  is positive; that is, compressional strain is defined negative in Eq. 3-10. The radius of local curvature is the reciprocal of the curvature  $\kappa$ . The expression of curvature is given by

$$\kappa = \frac{1}{R} = \frac{\left(\frac{d^2 w}{dx^2}\right)}{\left[1 + \left(\frac{dw}{dx}\right)^2\right]^{\frac{3}{2}}} \approx \frac{d^2 w}{dx^2} \quad (3-11)$$

If the slopes is small (as our assumption of  $w \ll L$ ), the denominator of Eq. 3-11 will reduce to 1. So the curvature is equal to the second differentiation of the

deflection. Substitute Eq. 3-10 with Eq. 3-11, and then we have

$$\varepsilon_{xx} = -y\kappa = -y \frac{d^2w}{dx^2} \quad (3-12)$$

In Fig. 3-2, this plate illustrates the conditions of stresses and strains. Because the plate is infinitely long in the  $z$  direction, it won't be stretched and compressed in this direction. Hence,  $\varepsilon_{zz} = 0$ . Moreover, the stress normal to the surface,  $\sigma_{yy}$ , can be set to 0 throughout since the plate is thin and is on the top. Thus, Eq. 3-1 and 3-3 will be rewritten as

$$\varepsilon_{xx} = \frac{1}{E} (\sigma_{xx} - \nu \sigma_{zz}) \quad (3-13)$$

$$\varepsilon_{zz} = \frac{1}{E} (\sigma_{zz} - \nu \sigma_{xx}) = 0 \quad (3-14)$$

Therefore, the fiber stress will be obtained:

$$\sigma_{xx} = \frac{E}{1-\nu^2} \varepsilon_{xx} = -\frac{Ey}{1-\nu^2} \frac{d^2w}{dx^2} \quad (3-15)$$

The integration of fiber stresses is called the bending moment  $M$ :

$$\begin{aligned} M &= \int_{-h/2}^{h/2} \sigma_{xx} y dy \\ &= \frac{-E}{1-\nu^2} \frac{d^2w}{dx^2} \int_{-h/2}^{h/2} y^2 dy \\ &= \frac{-Eh^3}{12(1-\nu^2)} \frac{d^2w}{dx^2} \end{aligned} \quad (3-16)$$

We define the coefficient as the flexural rigidity,  $D$ , because it is usually used:

$$D \equiv \frac{Eh^3}{12(1-\nu^2)} \quad (3-17)$$

Thus,

$$M = -D \frac{d^2w}{dx^2} \quad (3-18)$$

Substituting Eq. 3-18 into Eq. 3-9 gathers the most common formula of the deflection of the plate:

$$D \frac{d^4w}{dx^4} = q(x) - P \frac{d^2w}{dx^2} \quad (3-19)$$

Note that  $D$  (flexural rigidity) is the property of the material,  $q(x)$  is the summation of the vertical force, and  $P$  is the summation of the horizontal force. Both  $q$  and  $P$  are in unit of the  $z$  direction ( $Nm^{-1}$ ). Eq. 3-19 will be the most fundamental formula in the next discussion, which tries to apply the case of the equatorial ridge into the deflection equation.

### 3.3 Analytical Flexure Model of the Equatorial Ridge

The modeling of the ridge can be done analytically or numerically. In section 3.3, we will first discuss the accessibility and assumptions of the analytical flexural model. And in section 3.4, the numerical model will be introduced, including the differences between these two models.

#### 3.3.1 Material Properties of Iapetus

According to the fossil shape of Iapetus, the reasonable inner structure of Iapetus appears a stratified composition. The materials deform plastically so that Iapetus was reshaped to an oblate spheroid. But the surface appeared old since many craters have conserved. Therefore, early Iapetus must have an elastic surface which is cooler than the plastic inner layer when the equatorial ridge formed. This is a good condition fitting the flexure model.

First, we compute the pressure inside Iapetus in order to decide the material properties. The gravity in the distance  $r$  ( $r \leq R$ ) from the center of Iapetus is given by:

$$g(r) = \frac{G}{r^2} \frac{4}{3} \pi r^3 \rho \quad (3-20)$$

Upon Eq. 3-20, the pressure  $P(r)$  in the distance  $r$  from the center of Iapetus is calculated:

$$\frac{dP}{dr} = g(r) \rho \quad (3-21)$$

$$P(r = 0) = \int_0^R \frac{dP}{dr} dr = \int_0^R \frac{4G\pi r \rho^2}{3} dr = \frac{2}{3} G\pi R^2 \rho^2 \quad (3-22)$$

Eq. 3-22 reveals the pressure in the center of Iapetus is 89.2 MPa (using  $G = 6.67 \times 10^{-11} \text{ m}^3 \text{kg}^{-1} \text{s}^{-2}$ ). If it is assumed that the major composition of Iapetus is water ice, it is important that which phase of water ice could exist inside Iapetus. According to Fig. 3-5 which shows the phase diagram of water, the main factor affecting the phase change of water under the pressure of 89.2 MPa is temperature. When temperature is lower than 72K, water ice changes its face from hexagonal

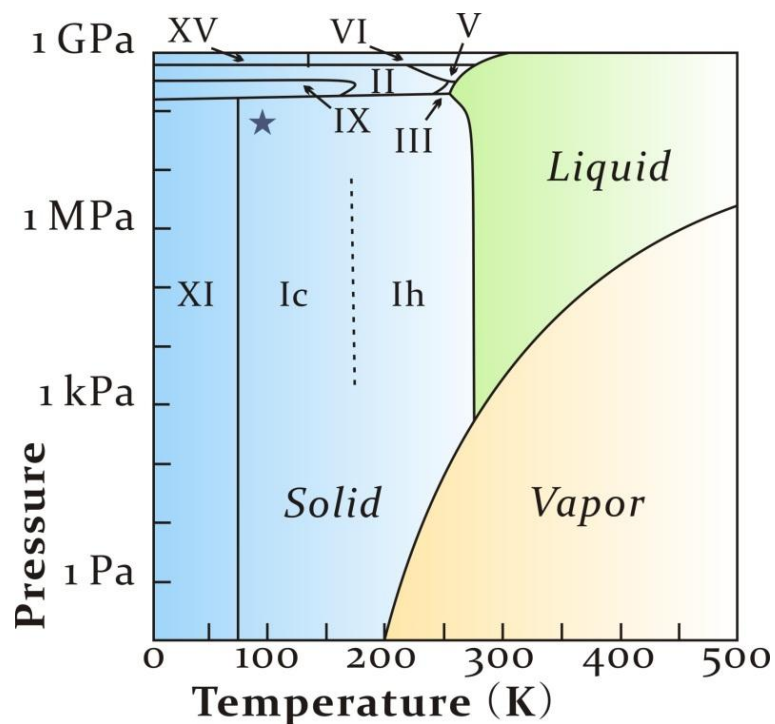
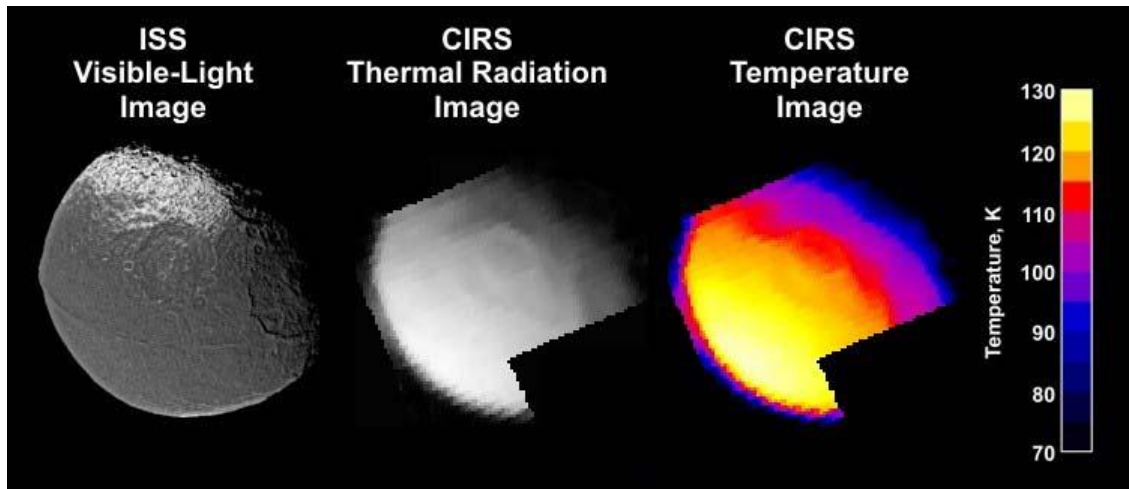


Fig. 3-5 The phase diagram of water. Modified from Chaplin (2012) (partly).

The roman numerals represent the different phase of water ice. Ice Ic is the metastable variant of Ih. The boundary temperature of ice XI and Ic is about 72K. The asterisk marks the possible P-T condition of Iapetus' core.



**Fig. 3-6 Iapetus thermal radiation image**, taken by the Cassini composite infrared spectrometer instrument (CIRS) on December 2004. PIA07004, Courtesy of NASA.

crystalline ice Ih to orthorhombic ice XI (Fukazawa *et al.*, 1998). The surface temperature obtained by Cassini thermal radiation instrument is shown in Fig. 3-6. The daytime temperature is ranged from 70 to 130K, and must be cooler in the nighttime since Iapetus has a slow spin rate. The modeling of inner thermal structure also suggested that the temperature near the surface of Iapetus is approximately 100K (Castillo-Rogez *et al.*, 2007). In the early stage of Iapetus, the surface would be hotter than the present day. Therefore, it is reasonable that setting the surface materials of Iapetus as ice Ih. Theoretically, the transition of Ice XI occurs when the temperature is 57-62K, which is equal to the temperature Uranus and Neptune are (Fukazawa *et al.*, 2006). But recent study implies a small amount of ice XI existence in the site of Jupiter and Saturn where the temperature is higher than 72K (Arakawa *et al.*, 2011). It is negligible that whether ice XI exists on Iapetus because of the small amount.

Briefly, the inner materials of early Iapetus shall be deformed plastically, while

the surface materials were bent elastically. These conditions are adequate to construct a flexure model, describing the deflection of the equatorial ridge. To simplify the properties of materials, we assume the bulk composition of Iapetus (including the ridge) is ice Ih; in the other words, we ignore the effects of the transition of the phase of water ice.

### 3.3.2 Basic Assumptions and Approximate Equations for the Ridge

In the 1-D analytical flexure model, the x direction is set to the direction normal to the stretching direction (z direction) of the equatorial ridge; that is, the N-S direction along the surface of Iapetus. The zero point of x-axis is the peak of the ridge. Before starting the modeling, this study sets 3 assumptions for the equatorial ridge in order to simplify the complexity of modeling. They will be described below:

1) The equatorial ridge is regarded as a mountain that perfectly surrounds Iapetus by its equator. Therefore, the ridge is laterally infinite, and the width of the ridge is small compare to its infinite length. According to this assumption, the load function can be reduced to a downward point load function plus an upward load due to the deflection:

$$q(x) = q_0 \delta(x) - \rho g w(x), \quad \delta(x) = \begin{cases} 1, & x = 0 \\ 0, & x \neq 0 \end{cases} \quad (3-23)$$

where  $q_0$  is the total load of the ridge per unit length in the z direction,  $\delta(x)$  is the delta function which is dimensionless. The first term in Eq. 3-23 ( $q_0 \delta$ ) describes the load due to the mass of the ridge, and the second term ( $-\rho g w$ ) states the force under the balance of hydrostatic equilibrium. The profile of the ridge is set to a

simple triangular, and the density of the ridge is uniform, equal to the density of Iapetus ( $1083 \text{ g/cm}^3$ ). Thus  $q_0$  can be evaluated in the following simple method:

$$q_0 = \frac{1}{2} HW \rho g \quad (3-24)$$

where  $H$  and  $W$  are the height and the width of the ridge separately. Both  $H$  and  $W$  vary with the local geomorphology, so the value of  $q_0$  changes when we use the different profiles of the ridge. The second part of Eq. 3-23 is the load due to the deflection, and Fig. 3-7 shows the origin of this load, which generates from the hydrostatic pressure of the deflected material.

2) The flexure model on an elastic shell of a planet should be described by the study of Beuthe (2008); however, the planar earth is useful for a thin shell compare to its radius. We assume that the elastic thickness ( $h$ ) is much smaller than the Iapetus' radius ( $R = 734.3 \text{ km}$ ; if an error of 5% is acceptable, the planar earth condition is compatible when  $h < 36.7 \text{ km}$ ). Therefore, the flexure model can be simplified without considering the effects of the elastic shell's curvature. After modeling, we will also proof whether this assumption is adaptable or not.

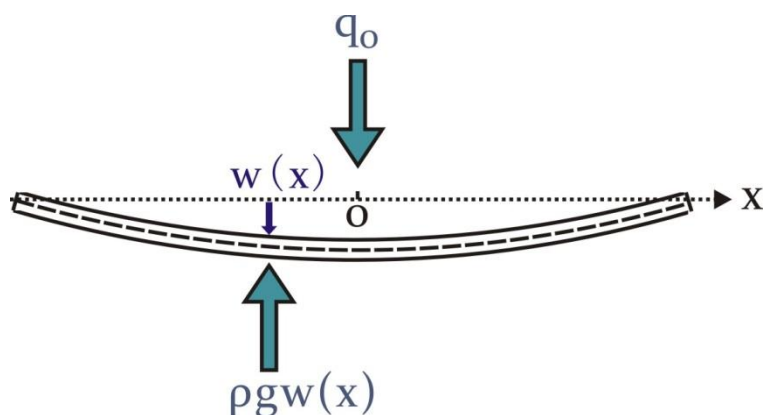


Fig. 3-7 Illustration of vertical forces on a deflected elastic plate.

3) Since the surface of Iapetus appears old according to section 2.1.2, it is reasonable that Iapetus may not have any tectonic activities in its entire lifespan. (Obviously, the equatorial ridge is the most doubtful structure created by plate tectonics, but this study ignores this possibility.) Based on this idea, the horizontal force  $P$  in Eq. 3-19 is set to zero.

Compiling these 3 assumptions, Eq. 3-19 can be rewritten to a brief form:

$$D \frac{d^4 w}{dx^4} + \rho g w = q_0 \delta(x) \quad (3-25)$$

Since the load function  $q(x)$  is always zero except  $x = 0$ , it can be treated as  $q(x) = 0$  on solving the differential equation. The general solution of Eq. 3-25 is

$$w = e^{Ax} (C_1 \cos Ax + C_2 \sin Ax) + e^{-Ax} (C_3 \cos Ax + C_4 \sin Ax), \quad (3-26)$$

$$A = \left( \frac{\rho g}{4D} \right)^{\frac{1}{4}} \quad (3-27)$$

Because  $P = 0$ , from Eq. 3-7 we have

$$\frac{dM}{dx} = V \quad (3-28)$$

The shear force  $V$  is half the amount of the vertical load  $q_0$  according to the static forces balance and the symmetric plate condition. There are 2 upward forces

$q_0/2$  at the lateral supports. By combining Eq. 3-28 and 3-18 and this idea, we find

$$\frac{d^3w}{dx^3} = -\frac{q_0}{2D} \quad (3-29)$$

Since the plate is symmetrical and is laterally bounded, the boundary conditions of Eq. 3-26 can be easily set as:

$$B.C. \begin{cases} w \rightarrow 0 \text{ as } x \rightarrow \pm\infty \\ w' = 0 \text{ at } x = 0 \\ w''' = \frac{-q_0}{2D} \text{ at } x = 0 \end{cases} \quad (3-30)$$

For substituting Eq. 3-30 into Eq. 3-26, it is obvious that  $c_1 = c_2 = 0$  and  $c_3 = c_4$ .

The particular solution is solved:

$$w = \frac{q_0}{8DA^3} e^{-Ax} (\cos Ax + \sin Ax) \quad (3-31)$$

This equation is fundamental in our analytical flexure modeling. It begins when the elastic thickness (required to compute  $D$  and  $A$  in Eq. 3-31) are given. Also, the shape (required to compute  $q_0$ ) of the ridge is based on the DTM data published by Giese, Denk *et al.* (2008). The results will be showed in the next chapter.

### 3.3.3 Modeling Flow Chart

The processes of the modeling are briefly described in the following flow chart. (Fig. 3-8)

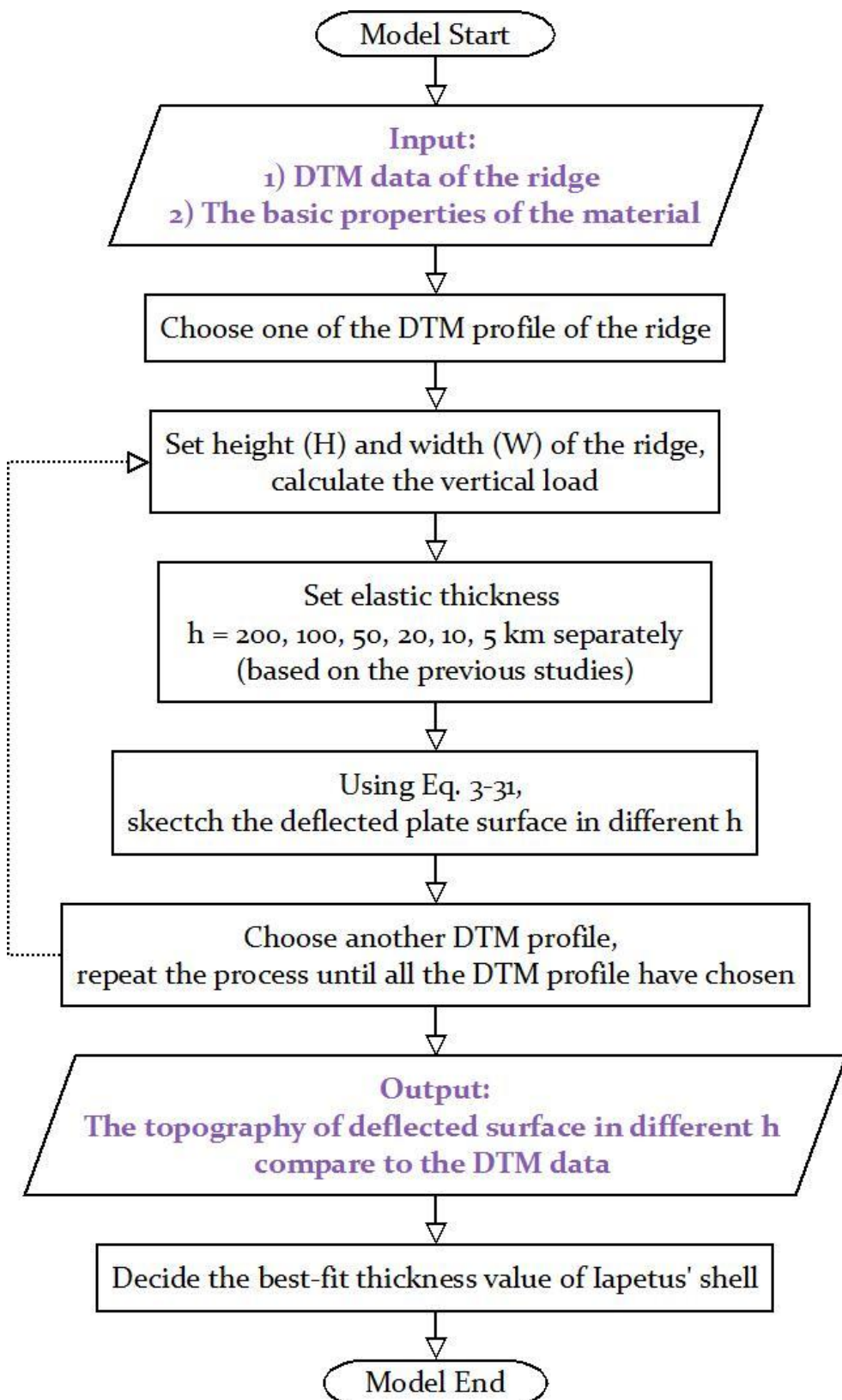


Fig. 3-8 Flow chart of the analytical flexural modeling.

## 3.4 Numerical Flexure Model of the Equatorial Ridge

### 3.4.1 Differences between Analytic and Numerical

The study also uses the numerical method for calculating the deflection more precisely. The fundamental formula is similar to Eq. 3-25, and listed below:

$$D \frac{d^4 w}{dx^4} + \rho g w = q(x) \quad (3-32)$$

It is assumed that the elastic thickness and the density of Iapetus do not change with  $x$ , so  $D$  and  $\rho g$  are constants. But the point load  $q(x)$  in Eq. 3-32 is replaced by a function related to the terrain data of the profile. The equation is solved numerically by the approach of the finite difference solution. If the  $x$ -grid and the deflection function  $w(x)$  for every grid block are set, the fourth differential term of  $w$  can be written as

$$\frac{d^4 w}{dx^4} = \frac{1}{h^4} (w_{i-2} - 4w_{i-1} + 6w_i - 4w_{i+1} + w_{i+2}) \quad (3-33)$$

where  $w_i = w(i)$ ,  $h$  is the width of the grid block. Therefore, the differential equation will transform to

$$\begin{aligned} Dw_{i+2} - 4Dw_{i+1} + (6D + \rho g h^4)w_i \\ - 4Dw_{i-1} + Dw_{i-2} = h^4 q_i \end{aligned} \quad (3-34)$$

where  $q_i = q(i)$ . Eq. 3-34 is also written as a symmetrical pentadiagonal matrix:

$$\begin{bmatrix} \alpha & \beta & \gamma & 0 & \cdots & 0 \\ \beta & \alpha & \beta & \gamma & & \vdots \\ \gamma & \beta & \ddots & \ddots & & 0 \\ 0 & \gamma & \ddots & \ddots & & \gamma \\ \vdots & \ddots & \ddots & \ddots & & \beta \\ 0 & \cdots & 0 & \gamma & \beta & \alpha \end{bmatrix} \begin{bmatrix} w_1 \\ w_2 \\ \vdots \\ w_n \end{bmatrix} = \begin{bmatrix} \delta_1 \\ \delta_2 \\ \vdots \\ \delta_n \end{bmatrix} \quad (3-35)$$

where  $\alpha = 6D + \rho gh^4$ ,  $\beta = 4D$ ,  $\gamma = D$ ,  $\delta_i = h^4 q_i$ . To solve  $w_i$  technically, We use the algorithm called LU decomposition. LU decomposition factorizes a symmetrical pentadiagonal matrix as the product of an upper triangular matrix and a lower triangular matrix. Hence, Eq. 3-35 would be solved numerically in efficiency.

The main modification of the numerical model from the analytic model is the input of load  $q(x)$ , but we also try a model with variable elastic thickness since Iapetus' shell may thicken or thin due to cratering. The model with variable  $h$  is referred to the flexure program published by Community Surface Dynamics Modeling System (CSDMS) Facility, Univ. of Colorado (which is published online, URL: <http://csdms.colorado.edu/wiki/Model:Flexure>; see Wickert (2012)). This study rewrites the program to adapt to the 1-D conditions of Iapetus.

### 3.4.2 Modeling Flow Chart

The processes of the constant-thickness numerical modeling are briefly described in the following flow chart (Fig. 3-9). Variable-thickness modeling has the similar processes except the input of  $h$  is replaced by the function of  $x$ .

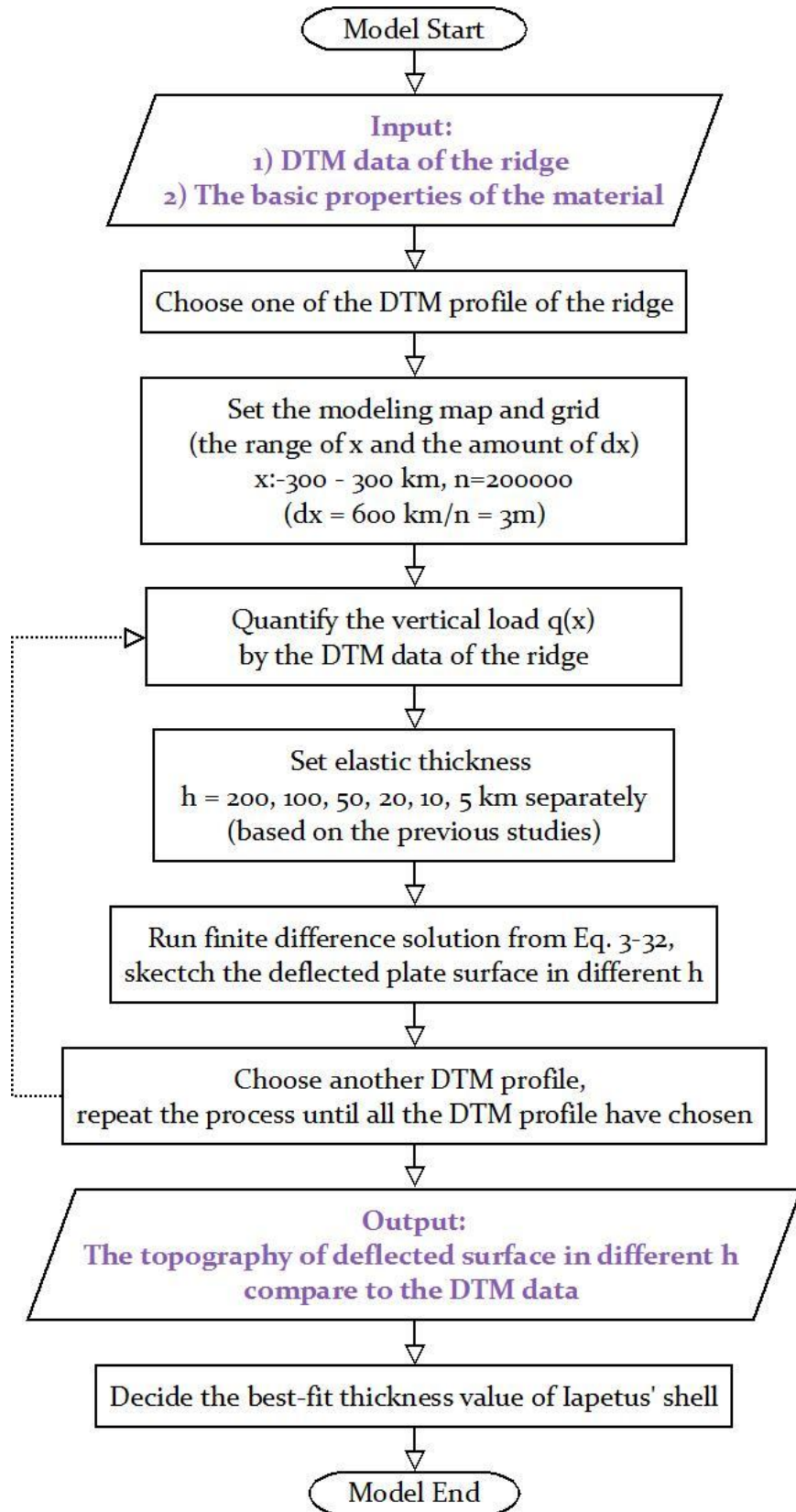


Fig. 3-9 Flow chart of the numerical flexural modeling.

### 3.5 Features against the previous studies of Iapetus' flexure model

Actually, there are several flexural studies for Iapetus before this paper. Giese, Denk *et al.* (2008) have estimated the elastic lithospheric thickness of the ridge area. They simplified the ridge as a disc-shaped load, and computed the deflection by the method suggested by Brotchie and Silvester (1969). Under the assumption that the deflection must be less than 1 km, they concluded that the thickness of the elastic lithosphere should be over 100 km. Moreover, Dombard *et al.* (2012) have modeled the flexure by numerical way. Since they argued that there is no flexure signal, the modeling outcome gave the value of heat flow of less than  $1 \text{ mW m}^{-2}$ , which is representative of a  $\sim 70$  km elastic thickness.

However, there are some suspected depression areas which may be caused by the deflection on the DTM profiles. The next chapter will show these profiles, and proof the possibility of deflection. It is the first discussion of Iapetus flexure using DTM data, and the previous studies may need renewing for a thin elastic thickness scenario.

## Chapter 4 Research Results

### 4.1 Analytical Solution

In the DTM data published by Giese, Denk *et al.* (2008), there are 10 profiles numbered r1 to r10, scattering on the Cassini Regio. The sites of the profiles are shown in Fig. 4-1. Profile r1 and r2 only lies on the northern side of the equatorial ridge, and the other profiles are cutting through the ridge. However, r9 is excluded from our modeling since the ridge area in r9 is devastated by cratering. In this study,

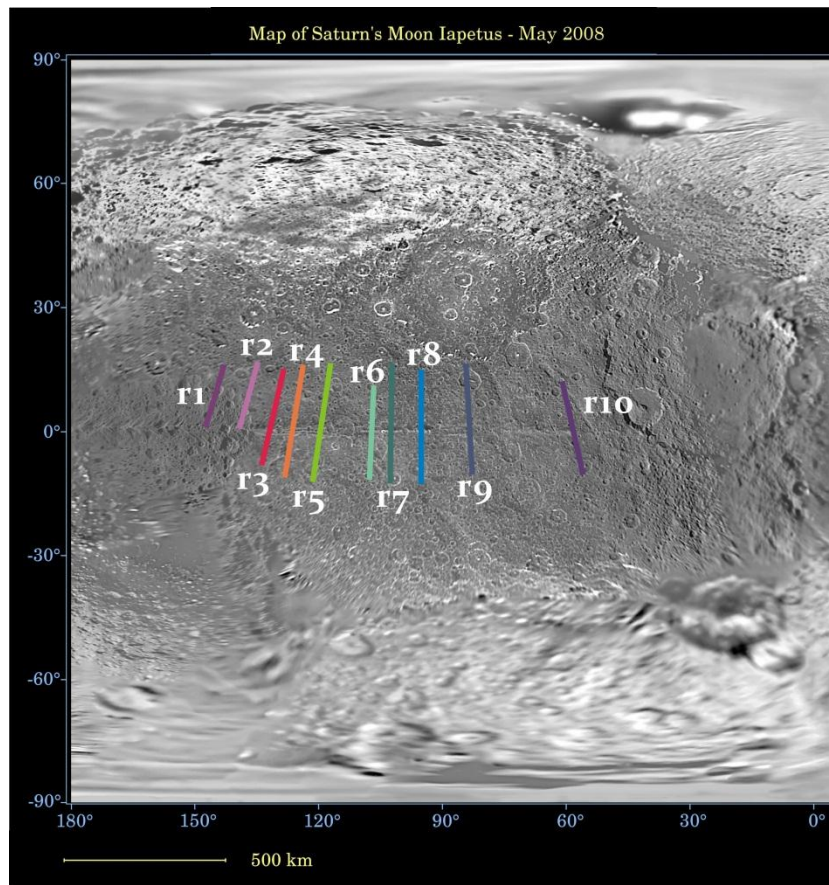


**Fig. 4-1 The site of DTM profiles.** Modified from PIA08406 (courtesy of NASA) and Giese, Denk *et al.* (2008).

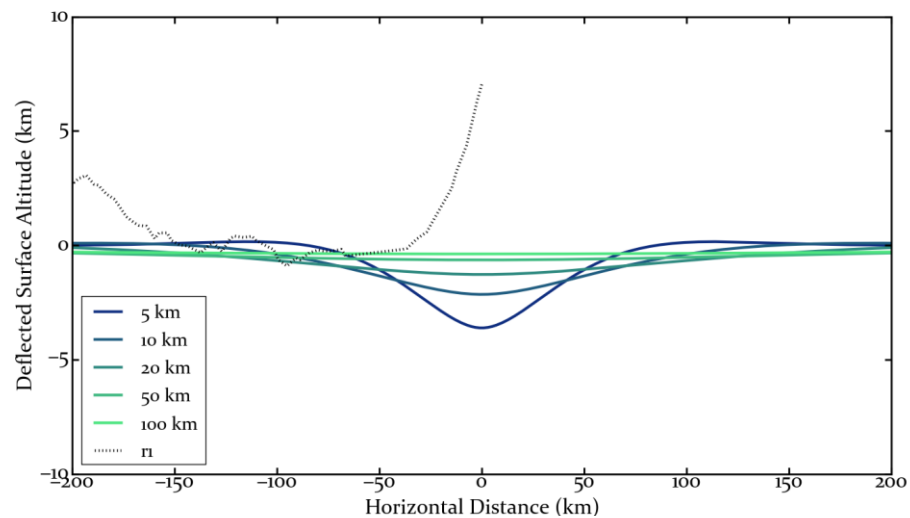
the excess load originated from the sunken part of the mountain is ignored in order to simplify condition setting. Thus, the estimated width (W) and height (H) of the ridge are obtained from the DTM profile, and then we use Eq. 3-24 to compute the vertical load ( $q_o$ ). The values of H, W and  $q_o$  for every profile are listed in Table 2. In the other hand, we select the basic properties of Iapetus' material below: density ( $\rho$ ) =  $1088 \text{ kg/m}^3$  (which is the same as the average density of Iapetus); Young's modulus =  $9 \times 10^9 \text{ Pa}$ , Poisson's ratio = 0.33 (both based on the study of ice published by Schulson (2001)).

**Table 3 Parameters of The Equatorial Ridge for Every Profile**

Profile Number	Ridge Width (km)	Ridge Height (m)	Vertical Load (N/m)
r1	74.8*	7032	$6.34 \times 10^{10}$
r2	119.2*	8983	$1.29 \times 10^{11}$
r3	98.4	6820	$8.09 \times 10^{10}$
r4	120.8	7158	$1.04 \times 10^{11}$
r5	117.6	6818	$9.66 \times 10^{10}$
r6	157.2	5604	$1.06 \times 10^{11}$
r7	167.5	6303	$1.27 \times 10^{11}$
r8	69.0	8398	$6.98 \times 10^{10}$
r10	63.5	6561	$5.02 \times 10^{10}$

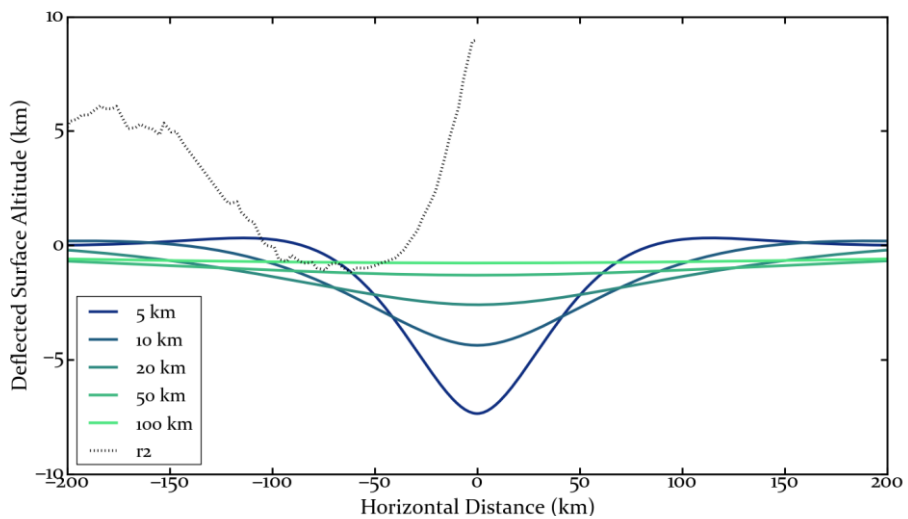
\*: The value is from the doubled width of the north wing because of the lack of DTM data of the ridge's southern wing.

Fig. 4-2 to 4-10 show the DTM ridge profile and the deflected surface. In the computation of the deflected surface, the elastic lithospheric thickness is set to 5, 10, 20, 50, 100, 200 km respectively. But these figures will show only up to 100-km thickness since an over 100-km thickness will not cause a significant deflection.



**Fig. 4-2 Analytical Flexural Modeling of Profile r1.**





**Fig. 4-3 Analytical Flexural Modeling of Profile r2.**

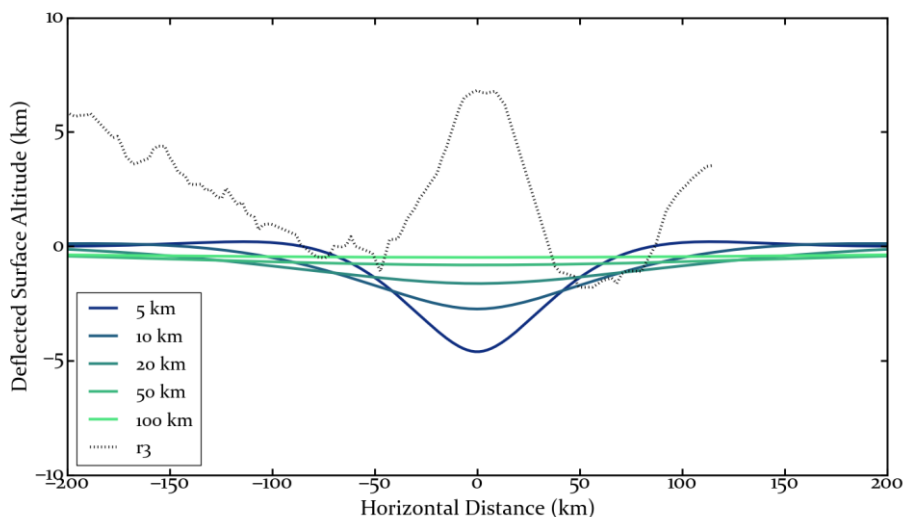


**Fig. 4-4 Analytical Flexural Modeling of Profile r3.**

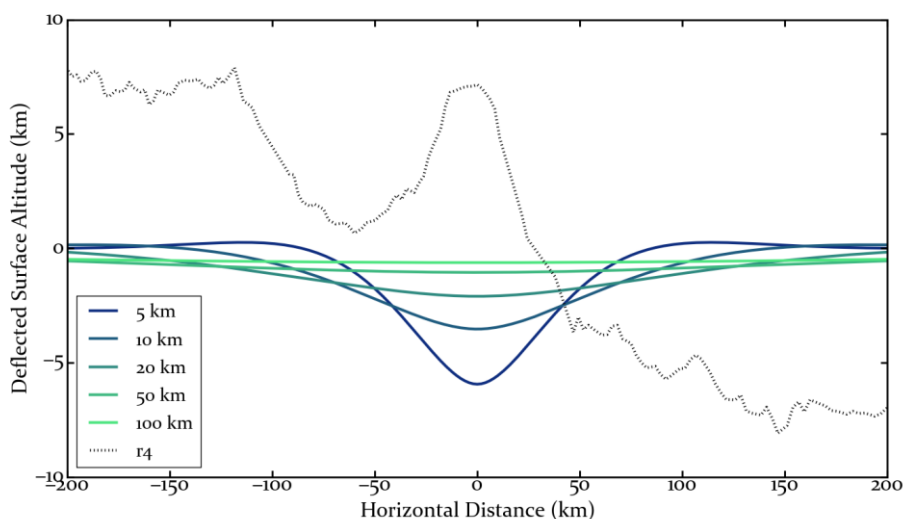


**Fig. 4-5 Analytical Flexural Modeling of Profile r4.**

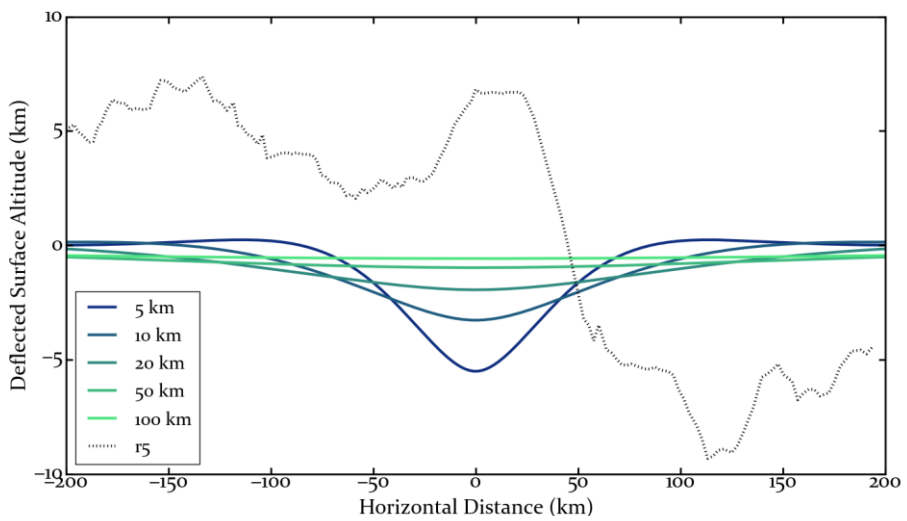


**Fig. 4-6 Analytical Flexural Modeling of Profile r5.**

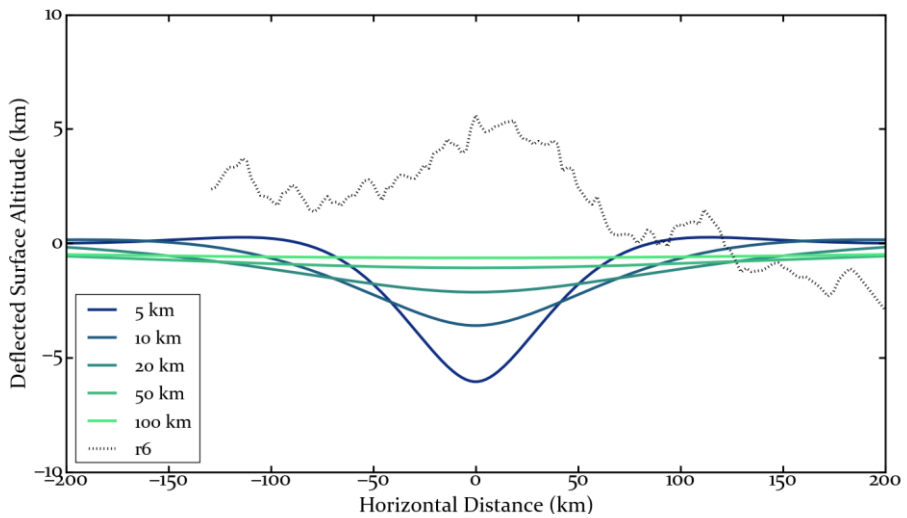


**Fig. 4-7 Analytical Flexural Modeling of Profile r6.**

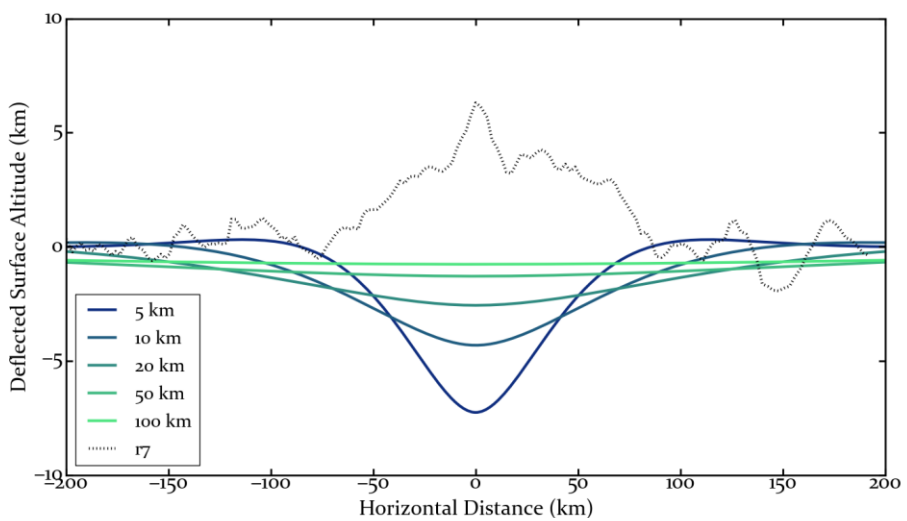


**Fig. 4-8 Analytical Flexural Modeling of Profile r7.**

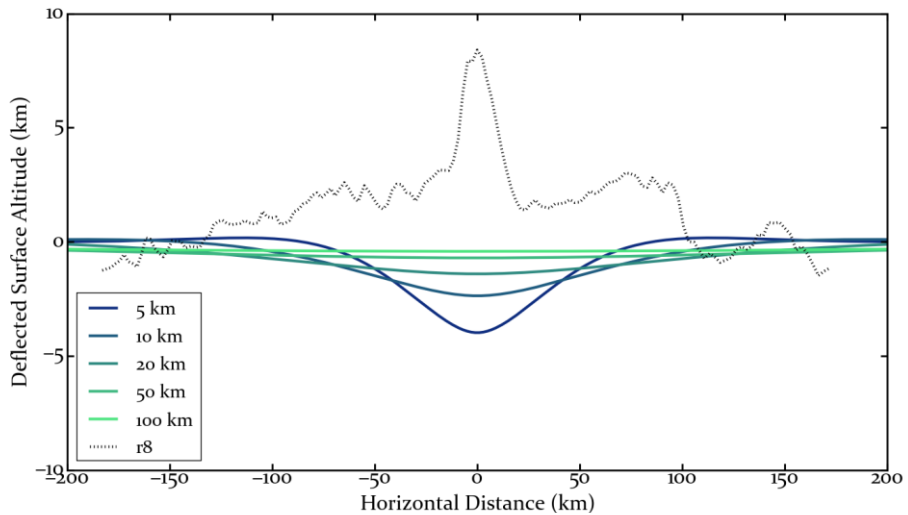


**Fig. 4-9 Analytical Flexural Modeling of Profile r8.**

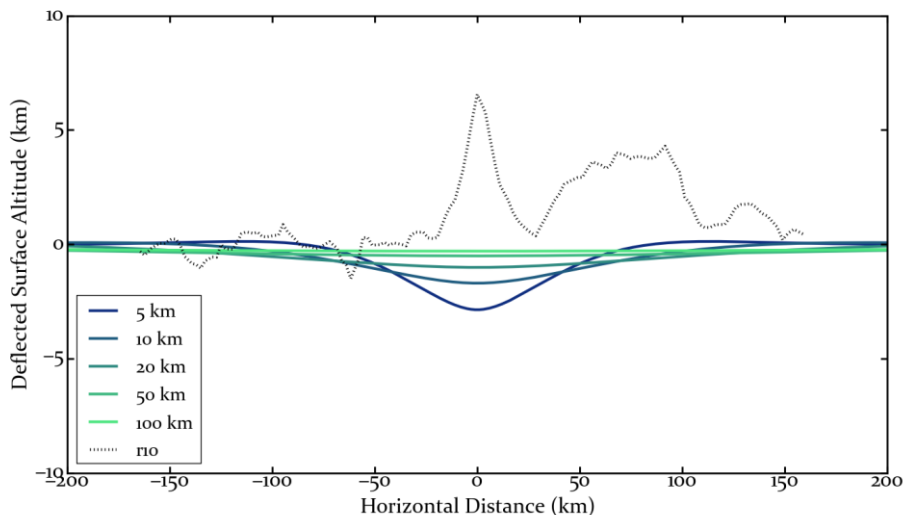


**Fig. 4-10 Analytical Flexural Modeling of Profile r10.**

These results show at least four noticeable truths:

- 1) The modeling results of 100-km elastic thickness agree with the previous studies (Dombard *et al.*, 2012; Giese, Denk *et al.*, 2008), proving the validity of the analysis model.
- 2) Every profile has a bulge at 70-120 km away from the equatorial ridge. The bulge position correlates with the modeling result of 5-km elastic thickness.
- 3) The height of the bulge ranges from 1 km (r6 & r7) to 7 km (r4). Obviously,

deflection causes a hundred-meter to 1-km high bulge, but cannot make an ultrahigh uplift. The high bulge is not simply originated from the point load of the ridge.

4) Except the ridge and the bulges, most of the surfaces are affected by the impact craters. For instance, a 3-km deep crater is located in the southern side of profile r8. Large crater directly changed the surface topography a lot, and r4 is the good example since its southern side was devastated by a large impact event. Such a large event would destroy any previous flexure signal caused by the ridge.

#### 4.1.1 Geomorphological Constraints of Elastic Thickness

In fact, we can estimate the elastic lithospheric thickness by the distance between the bulge and the loading point. The peak of the bulge has the distance away from the ridge of 100-200 km from the each profile.

Upon differentiating Eq. 3-31 and setting the result to 0, the x value that yields the maximum w value is obtained:

$$\frac{dw}{dx} = \frac{-q_0}{4DA^2} e^{-Ax} \sin Ax = 0 \quad (4-1)$$

$$x = \frac{\sin^{-1} 0}{A} = \frac{\pi}{A} = \pi \left( \frac{4D}{\rho g} \right)^{\frac{1}{4}} = \pi \left[ \frac{Eh^3}{3\rho g(1-\nu^2)} \right]^{\frac{1}{4}} \quad (4-2)$$

Substituting x from  $1 \times 10^5$  m to  $2 \times 10^5$  m into Eq. 4-2 and considering the appropriate variability of Young's modulus from  $10^{10}$  to  $10^9$  Pa yields the proper range of the elastic thickness with 5-10 km. Thus, if the bulge is made by the ridge load, the elastic thickness should be much thinner than the previous studies. It is significant because the first modeling using DTM data (this study) overrides the

former elastic lithosphere calculation on Iapetus. We will discuss more, including the outcomes and deduction in the next chapter.

## 4.2 Numerical Solution

### 4.2.1 Uniform Thickness

The numerical flexural model of the equatorial ridge has been done in the same material conditions with the analytical model mentioned in section 4.1. The length in our 1-D model is set to 300 km spanning from the both side of the ridge. (That is, the total length is 600 km.) In a numerical analysis with a boundary-conditioned differential problem, the amount of the map grid enlarges or shrinks the value of the solution. So, we compare the analytical and the numerical solution under the same condition (point load) as a pre-test. After the pre-test, the amount of the map grid is set to 200000 because it correlates well with the analytical model. The width of every grid is 3 m (600 km / 200000 grid points). Fig. 4-11 to 4-19 will show the computed deflected surface of the ridge profile separately. The dashed line indicates the load map ( $q(x)$ ) the numerical model used. Note that these figures don't show the deflected curves originating from 50-km, 100-km and 200-km elastic shell since these curves are so flat that the flexure effect can be ignored.

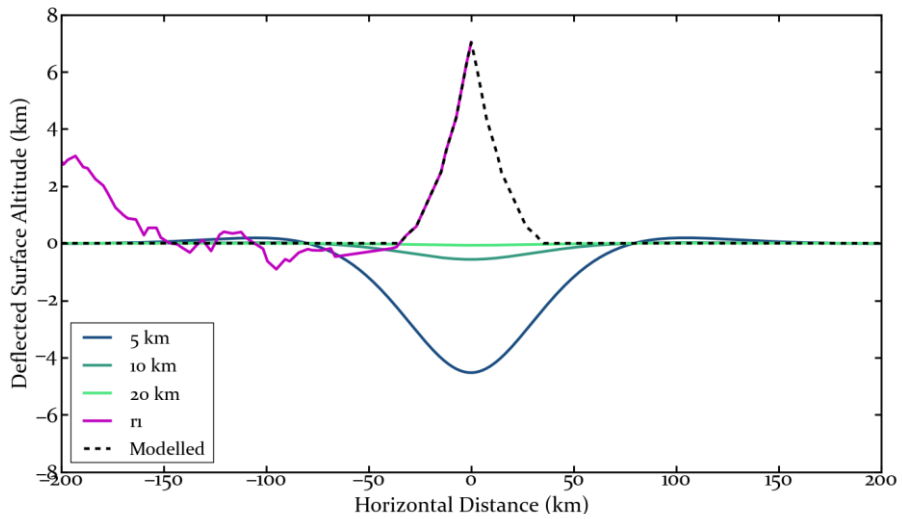


**Fig. 4-11 Numerical Flexural Modeling of Profile r1.**

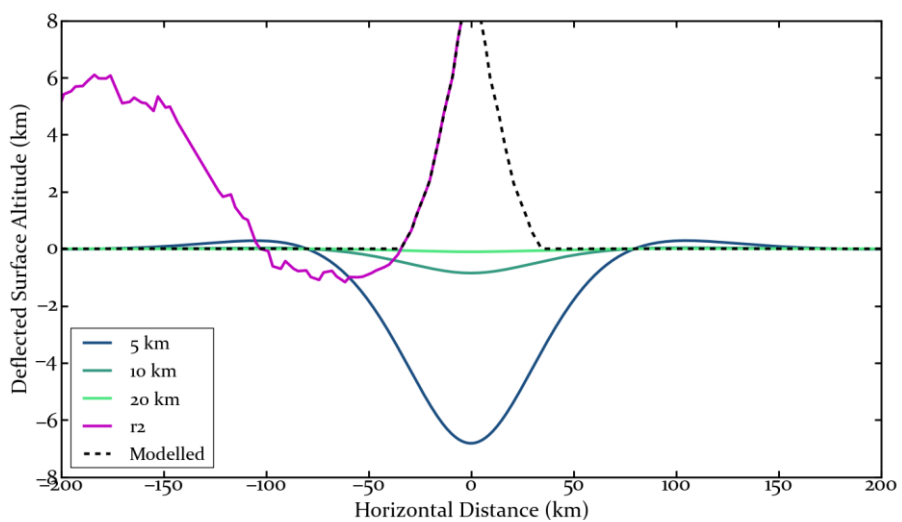


**Fig. 4-12 Numerical Flexural Modeling of Profile r2.**

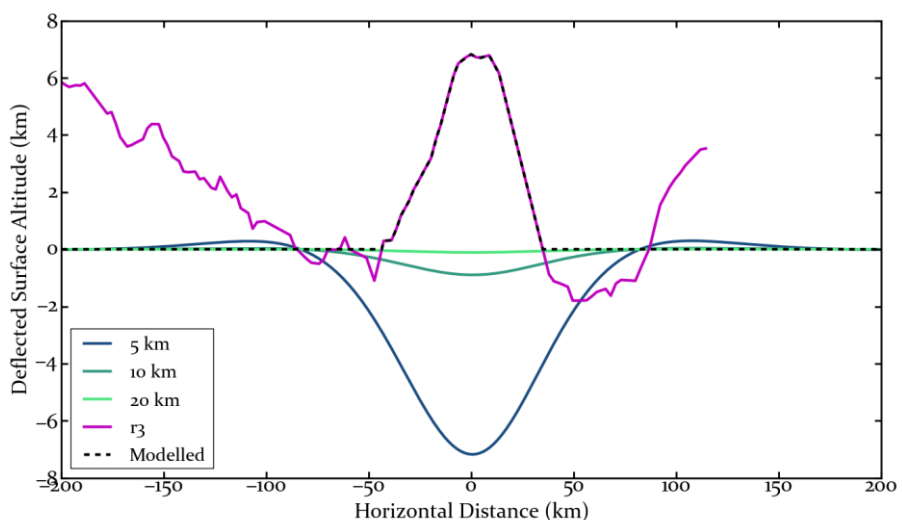


**Fig. 4-13 Numerical Flexural Modeling of Profile r3.**

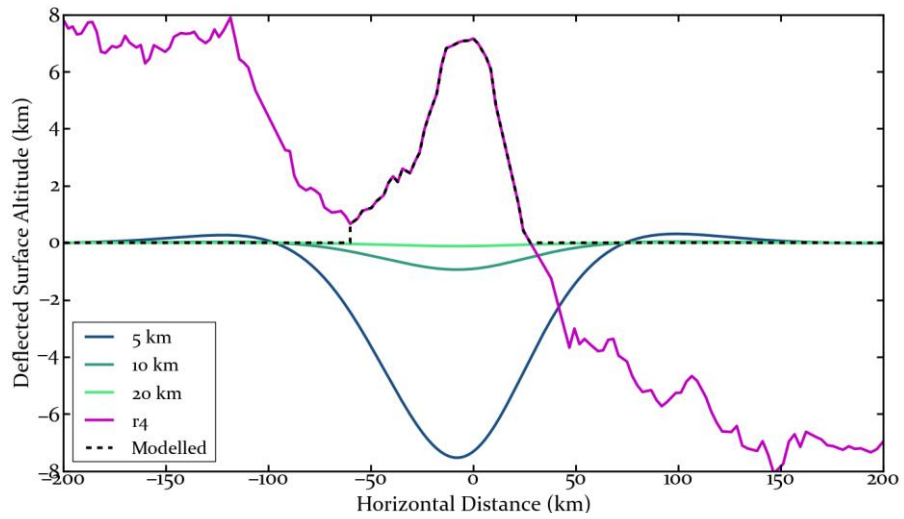


**Fig. 4-14 Numerical Flexural Modeling of Profile r4.**

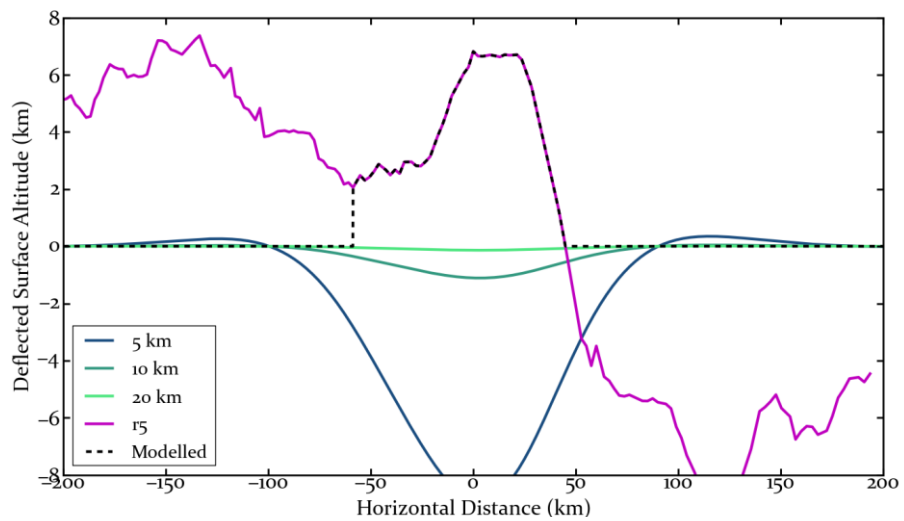


**Fig. 4-15 Numerical Flexural Modeling of Profile r5.**

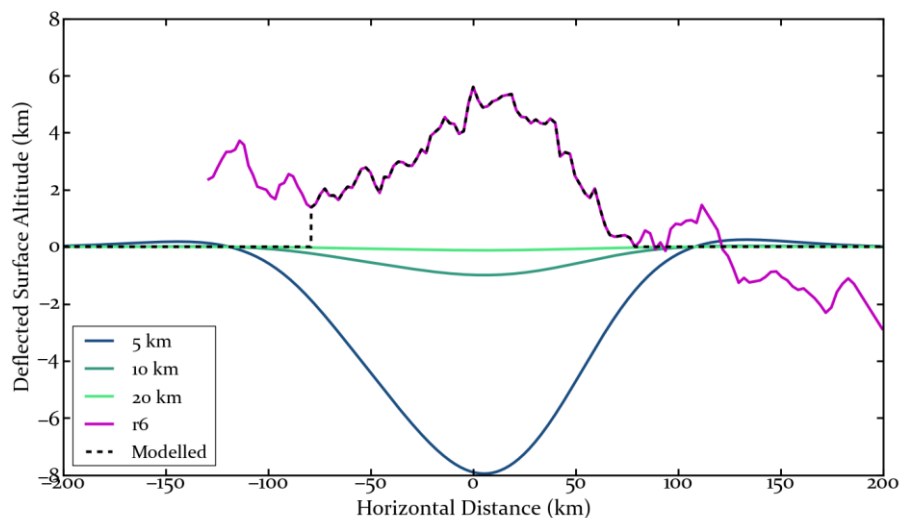


**Fig. 4-16 Numerical Flexural Modeling of Profile r6.**

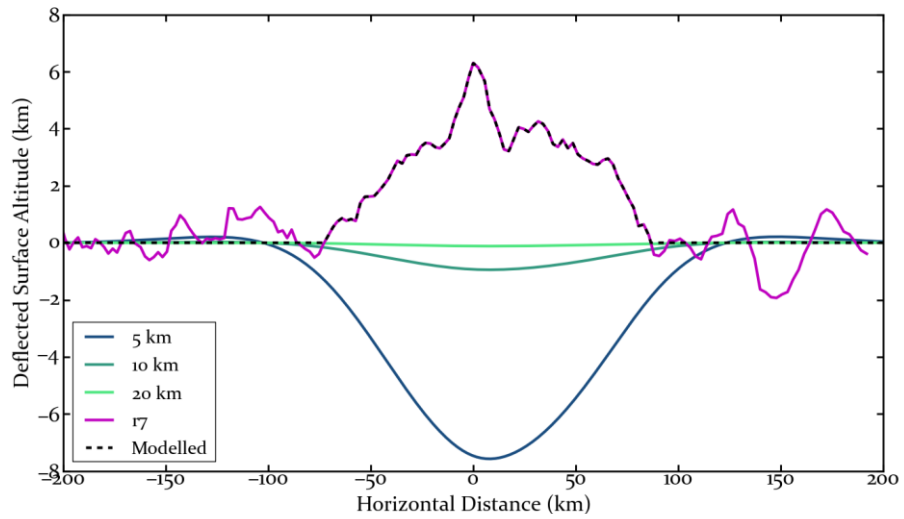


**Fig. 4-17 Numerical Flexural Modeling of Profile r7.**

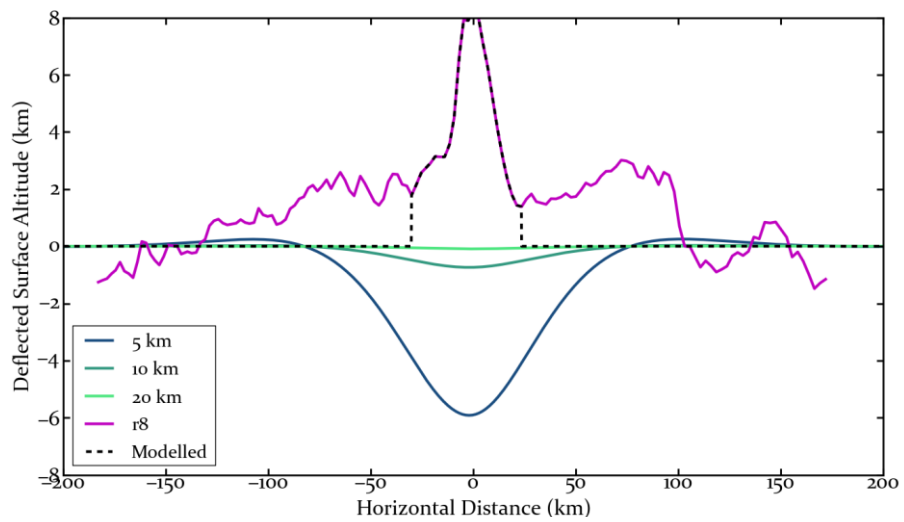


**Fig. 4-18 Numerical Flexural Modeling of Profile r8.**

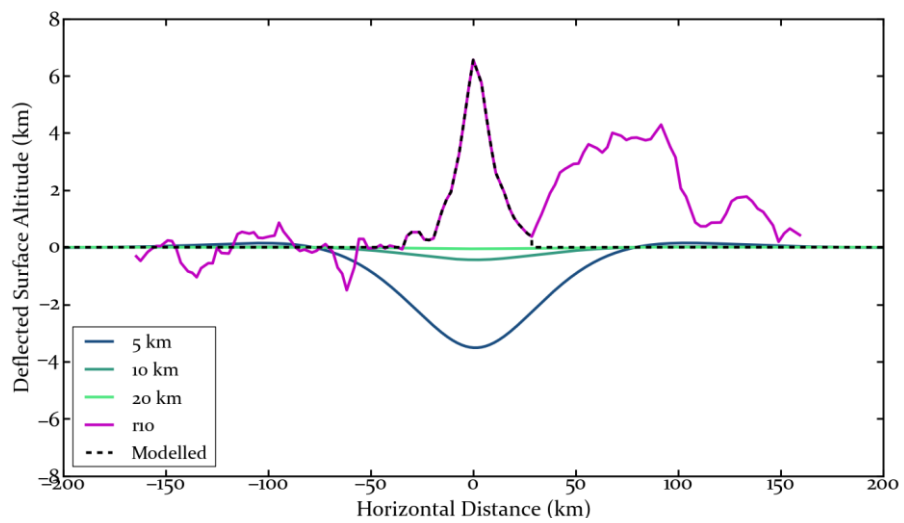


**Fig. 4-19 Numerical Flexural Modeling of Profile r10.**

Because of the bounded edges, the numerical results react smoother than the analytical results. But the bulge area appears in the same position with former results. Moreover, the characteristics of the finite element method is amplifying the highly deflected part and flattening the minor deflected part. So, deflection caused by over 20-km elastic layer is hardly observed.

#### 4.2.2 Variable Thickness

In the cratered ridge scenario, the impact would have heated Iapetus' surface. Therefore, the elastic lithospheric thickness would have been thinned, or more critically, decreased to zero. In this paper, we use r4 profile as an example of the scenario. A large crater is located on the south of the profile (e.g. Fig. 4-5). Hence, we set the elastic thickness to 5 km for the northern side and 1 km for the southern side of the ridge. Under the same material properties mentioned before, the modeling result is illustrated in Fig. 4-20.

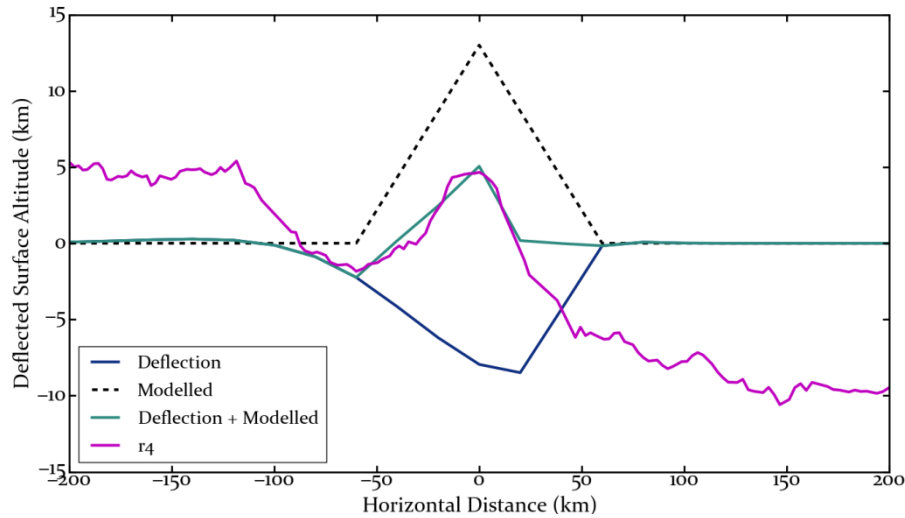


**Fig. 4-20 Modeling of Profile r9 with Various Lithospheric Elastic Thickness.**

In Fig. 4-20, the shape of the ridge is simplified to a symmetrical triangular with a height of 13 km and a width of 120 km (shown as a dashed line on Fig. 4-20). The modeled surface is highly correlated with the ridge area in r4 profile, so it's plausible that the profile was created by 2 factors: flexure and cratering. Deflecting can form the depression of the northern ridge, and an asteroid heavily bombarded the southern part of the ridge. But the most northern bulge "plateau" area remains unexplainable since it's too high to be constructed by only flexure. More details of numerical modeling will also be discussed in the next chapter.



## Chapter 5 Discussion and Conclusion

### 5.1 Interpretation of the Results

#### 5.1.1 Ridge Area

The flexure signals give us a hint that the elastic thickness is about 5-10 km. The modeling results also show that the maximum value of deflection with a 5-10 km thickness varies from 3-7 km. This situation gives us an implication: the original equatorial ridge would be higher than the present ridge. The average height of the present ridge is ~7 km, so the original height of the ridge may reach over 10-14 km. using a wing width of 37.4 km (profile r1) yields the average slope of the original ridge of 15-20 degrees. It becomes a hint on determining the proper model of the origin of the equatorial ridge, and will be discussed in section 5.2.2.

#### 5.1.2 Ultrahigh Bulge

The existence of the bulge is the powerful evidence for flexural signals. Most of the profiles have its bulges that represent for the flexure with an elastic thickness of 5-10 km. (See section 4.1 and 4.1.1.) But the height of bulge ranges a lot, from ~1 km to the maximum of 7 km. No evidence for the other reason causes the ultrahigh bulge, except flexure. However, Flexure contributed only by vertical loading is not sufficient to make the high bulge. As proved in Chapter 4, the height of the bulge caused by the flexure of vertical loading is limited to ~1 km. So, we must consider the other forces that generated deflection. There are still 2 possibilities: one is the tectonic horizontal force, another is the horizontal force induced by cratering. Due

to the lack of tectonic linear structure and the non-renewing surface, it's less possible that the tectonic force buckled the high bulge. On the other hand, cratering may play a significant role on the formation of the ridge since Iapetus' surface is mostly occupied by numerous craters.

R2 profile is just an example for the bulge's origin. From Fig. 2-2, large multiple craters (No.1 and No.4 crater in Fig. 2-2) lie on the northeast of the r2 profile. In general, the crater rim is higher than the original surface since the rim may be pushed by the impact pressure and be stuffed by impact ejecta (Melosh, 1996). And then, the northern side of the profile r2 is just located on the crater rim of crater No. 1. Therefore, the ultrahigh bulge may be caused by the large impact event, not the loading of the ridge. This interpretation is also useful to r3, r4 and r5 profile because they are in the same relative position of crater No. 1.

### 5.1.3 Craters

Impact crater is a powerful material for determining the age of the equatorial ridge. From Fig. 2-2, Crater No. 2 obviously truncated the ridge and totally devastated it. The other example is between profile r5 and r6 (right side of profile A-A' in Fig. 2-2) although this crater is smaller. The truth tells us that some impact events happened after the ridge formed. However, we don't find any craters which seem to be truncated by the ridge. Crater No. 5 is the potential one since its northern rim, which adjoins the ridge, is steeper than the other direction; but it is not sufficient to be evidence for the truncated crater. So, if we assume the age of Iapetus' surface is 4400 Myr which has been discussed in section 2.1.2, the ridge may be little younger than this age but not too much since a young ridge has a larger

possibility of truncating a crater. This idea will be a hint on the chronology of Iapetus; we are going to discuss more in section 5.3.

## 5.2 Formation Model of the Equatorial Ridge

Until now, we have proposed that the depression and the bulge of Iapetus' surface might be caused by ridge flexure on a thin elastic shell. This thin-shell model also offers constraints on the formation theory of the equatorial ridge. In this section, we will discuss these constraints and infer the proper model for ridge origin.

### 5.2.1 Possibility of a Thin Elastic Shell

This study suggests that the elastic lithospheric thickness of Iapetus is only 5-10 km when the ridge formed; the value is about one twentieth to the previous study (Giese, Denk *et al.*, 2008; Sandwell & Schubert, 2010). Is it possible that there was a thin elastic shell on Iapetus? To solve the question, we start from the thermal history of Iapetus. If the thermal flux was high, the surface of Iapetus would be more plastic, and then the elastic shell was thinner. In the early stage of Iapetus, the abundance of SLRI (short-lived radioactive isotopes, see section 2.1.4) was possibly high. Therefore, if the ridge formed in this period (200-1000 Myr after Iapetus formed, and before the synchronizing of Iapetus), the thermal flux generated by radioactive decay of SLRI was enough to maintain such a thin elastic layer. This idea is correlated with the observations of the ancient surface and the truncation relationship between craters and the ridge. All evidence implies that the ridge is an old structure formed in the very beginning stage of Iapetus.

In a nutshell, there are 2 factors supporting the hypothesis of the thin elastic layer. One is the depressed surface and the bulge areas on Iapetus, and another is the correlation between the formation time and the thermal flux.

### 5.2.2 Endogenic or Exogenic?

We are about to reexamine the origin model of the equatorial ridge. From the discussion of the previous section, the ridge was possibly formed when the thermal flux was high. Thus, the endogenic buckling model doesn't adapt to this condition since it needs a thick elastic layer. However, flexure model has less relationship with the other endogenic model such as the convection model. Therefore, Flexure model would not determine whether the ridge formation is endogenic or not.

On the other hand, flexure model has enhanced the possibility of the exogenic hypotheses that the ridge is supposed to be constructed by the ring remnant. This is because the result of this study tells us that the original slope of the ridge may be steeper than present. When the ring particles deposited on the surface of Iapetus, the slope of the pile would reach the angle of repose. Recent study suggested that when the gravity is reduced, the dynamic angle of repose decreases (Kleinhans *et al.*, 2011). According to this study, the dynamic angle of repose on Iapetus is only 20-30 degrees. If we assume the original slope of the ridge is 15-20 degrees as discussed in section 5.1.1, it would be more possible that the ridge was constructed by the ring particles. So, the result of the study shows the tendency of an exogenic origin of the equatorial model. But the mechanics of the ring formation (accretion disk or impact splash) remains unknown.

### 5.3 Chronology of Iapetus

Iapetus has 2 significant geological events: 1) the formation of the equatorial ridge; 2) the formation of the fossil 16-h shape. We have discussed the time constraints on these 2 events. These implications conclude to a time series of the geological events on Iapetus. The chronology is listed below:

- 1) Iapetus formed from the solar nebula 4567 Myr ago, accompanying Saturn and the other planets in the Solar System.
- 2) Ridge has formed several hundred million years after the formation of Iapetus. In this time, the SLRI inside Iapetus generated sufficient heat to maintain a thin elastic outer shell.
- 3) Iapetus was despinning because of the tidal locking of the Saturn. In the same time, the heat from SLRI was reducing. After the ridge formed, the 16-h shape of oblate spheroid was fixed due to the cooling down of the Iapetus' inner core. However, we cannot sure the time scale between the formation of the ridge and the formation of fossil shape.
- 4) Iapetus was totally synchronized with Saturn ~1000 Myr after the formation of Iapetus.
- 5) No obvious geological events except cratering happened on Iapetus after synchronizing.

## 5.4 Conclusion

Iapetus is the only object that has the equatorial ridge in the Solar System. In this study, we use the DTM data and the assumptions of the early-time Iapetus to construct the elastic lithospheric flexure model. Both analytical and numerical models are proposed in this study, giving similar results. The research results show that the elastic thickness of Iapetus' outer shell is 5-10 km when the ridge formed. It seems to contradict the earlier studies since these studies suggested that the elastic thickness must be over 100 km, but our study fits more observational data:

- 1) Depression and bulge areas around the ridge are interpreted as a deflection caused by the loading of the ridge acted on the thin elastic layer.
- 2) Studies on the thermal history of Iapetus also suggested that Iapetus once had the sufficient heat to maintain a thin elastic shell and a big portion of plastic inner core.

This result also gives an inference on the exogenic origin of the equatorial ridge. The ridge may be a rubble pile deposited by an ancient ring (Dombard *et al.*, 2012; Ip, 2006; Levison *et al.*, 2011), which is similar to the scene happened on another Saturnian satellite, Rhea (Schenk *et al.*, 2011). And the last, we give a chronology of important geological events on Iapetus. Our research supports that ridge formation is earlier than the fixing of fossil 16-h shape. All of these constraints will help us understanding the most peculiar mountain in our Solar System.

## Chapter 6 References

Amelin, Y., Krot, A. N., Hutcheon, I. D., & Ulyanov, A. A. (2002). Lead isotopic ages of chondrules and calcium-aluminum-rich inclusions. *Science*, 297(5587), 1678-1683.

Arakawa, M., Kagi, H., Fernandez-Baca, J. A., Chakoumakos, B. C., & Fukazawa, H. (2011). The existence of memory effect on hydrogen ordering in ice: The effect makes ice attractive. *Geophysical Research Letters*, 38.

Beuthe, M. (2008). Thin elastic shells with variable thickness for lithospheric flexure of one-plate planets. *Geophysical Journal International*, 172(2), 817-841.

Brotchie, J. F., & Silvester, R. (1969). On Crustal Flexure. *Journal of Geophysical Research*, 74(22), 5240-5252.

Buratti, B. J., Cruikshank, D. P., Brown, R. H., Clark, R. N., Bauer, J. M., Jaumann, R., McCord, T. B., Simonelli, D. P., Hibbitts, C. A., Hansen, G. B., Owen, T. C., Baines, K. H., Bellucci, G., Bibring, J.-P., Capaccioni, F., Cerroni, P., Coradini, A., Drossart, P., Formisano, V., Langevin, Y., Matson, D. L., Mennella, V., Nelson, R. M., Nicholson, P. D., Sicardy, B., Sotin, C., Roush, T. L., Soderlund, K., & Muradyan, A. (2005). Cassini Visual and Infrared Mapping Spectrometer Observations of Iapetus: Detection of CO<sub>2</sub>. *The Astrophysical Journal*, 622(2), L149-L152.

Castillo-Rogez, J. C., Johnson, T. V., Lee, M. H., Turner, N. J., Matson, D. L., & Lunine, J. (2009). 26Al decay: Heat production and a revised age for Iapetus. *Icarus*, 204(2), 658-662.

Castillo-Rogez, J. C., Matson, D. L., Sotin, C., Johnson, T. V., Lunine, J. I., & Thomas, P. C. (2007). Iapetus' geophysics: Rotation rate, shape, and equatorial ridge. *Icarus*, 190(1), 179-202.

Chaplin, M. (2012). Water Phase Diagram, from <http://www.lsbu.ac.uk/water/phase.html>

Cruikshank, D. P., Meyer, A. W., Brown, R. H., Clark, R. N., Jaumann, R., Stephan, K., Hibbitts, C. A., Sandford, S. A., Mastrapa, R. M. E., Filacchione, G., Ore, C. M. D., Nicholson, P. D., Buratti, B. J., McCord, T. B., Nelson, R. M., Dalton, J. B., Baines, K. H., & Matson, D. L. (2010). Carbon dioxide on the satellites of Saturn: Results from the Cassini VIMS investigation and revisions to the VIMS wavelength scale. *Icarus*, 206(2), 561-572.

Czechowski, L., & Leliwa-Kopystyński, J. (2008). The Iapetus's ridge: Possible explanations of its origin. *Advances in Space Research*, 42(1), 61-69.

Denk, T., Matz, K.-D., Roatsch, T., Wolf, U., Wagner, R. J., Neukum, G., & Jaumann, R.

(2000). *Iapetus (1): Size, Topography, Surface Structures, Craters*. Paper presented at the 31st Lunar and Planetary Science Conference, Houston, Texas.

Dobrovolskis, A. R., Peale, S. J., & Harris, A. W. (1997). Dynamics of the Pluto-Charon Binary. In S. A. Stern & D. J. Tholen (Eds.), *Pluto and Charon* (pp. 159). Tucson, AZ: Univ. of Arizona Press.

Dombard, A. J., & Cheng, A. F. (2008). *Constraints on the Evolution of Iapetus from Simulations of Its Ridge and Bulge*. Paper presented at the 39st Lunar and Planetary Science Conference, League City, Texas.

Dombard, A. J., Cheng, A. F., McKinnon, W. B., & Kay, J. P. (2012). Delayed formation of the equatorial ridge on Iapetus from a subsatellite created in a giant impact. *Journal of Geophysical Research*, 117(E3).

Fukazawa, H., Hoshikawa, A., Ishii, Y., Chakoumakos, B. C., & Fernandez-Baca, J. A. (2006). Existence of ferroelectric ice in the universe. *Astrophysical Journal*, 652(1), L57-L60.

Fukazawa, H., Ikeda, S., & Mae, S. (1998). Incoherent inelastic neutron scattering measurements on ice XI; the proton-ordered phase of ice I-h doped with KOH. *Chemical Physics Letters*, 282(2), 215-218.

Giese, B., Denk, T., Neukum, G., Roatsch, T., Helfenstein, P., Thomas, P. C., Turtle, E. P., McEwen, A., & Porco, C. C. (2008). The topography of Iapetus' leading side. *Icarus*, 193(2), 359-371.

Giese, B., Neukum, G., Roatsch, T., Denk, T., & Porco, C. C. (2006). Topographic modeling of Phoebe using Cassini images. *Planetary and Space Science*, 54(12), 1156-1166.

Giese, B., Wagner, R., Hussmann, H., Neukum, G., Perry, J., Helfenstein, P., & Thomas, P. C. (2008). Enceladus: An estimate of heat flux and lithospheric thickness from flexurally supported topography. *Geophysical Research Letters*, 35(24).

Gladman, B., Quinn, D. D., Nicholson, P., & Rand, R. (1996). Synchronous locking of tidally evolving satellites. *Icarus*, 122(1), 166-192.

Ip, W. H. (2006). On a ring origin of the equatorial ridge of Iapetus. *Geophysical Research Letters*, 33(16).

Jacobson, R. A., Antreasian, P. G., Bordi, J. J., Criddle, K. E., Ionasescu, R., Jones, J. B., Mackenzie, R. A., Meek, M. C., Parcher, D., Pelletier, F. J., Owen, W. M., Roth, D. C., Roundhill, I. M., & Stauch, J. R. (2006). The gravity field of the saturnian system from satellite observations and spacecraft tracking data. *The Astronomical Journal*, 132(6), 2520-2526.

Jet Propulsion Laboratory. (2007). Iapetus 049IA Mission Description: California Institute of Technology.

Jones, G. H., Roussos, E., Krupp, N., Beckmann, U., Coates, A. J., Crary, F., Dandouras, I., Dikarev, V., Dougherty, M. K., Garnier, P., Hansen, C. J., Hendrix, A. R., Hospodarsky, G. B., Johnson, R. E., Kempf, S., Khurana, K. K., Krimigis, S. M., Kruger, H., Kurth, W. S., Lagg, A., McAndrews, H. J., Mitchell, D. G., Paranicas, C., Postberg, F., Russell, C. T., Saur, J., Seiss, M., Spahn, F., Srama, R., Strobel, D. F., Tokar, R., Wahlund, J. E., Wilson, R. J., Woch, J., & Young, D. (2008). The dust halo of Saturn's largest icy moon, Rhea. *Science*, 319(5868), 1380-1384.

Kerr, R. A. (2008). Saturn's rings look ancient again. *Science*, 319(5859), 21.

Kirchoff, M. R., & Schenk, P. (2010). Impact cratering records of the mid-sized, icy saturnian satellites. *Icarus*, 206(2), 485-497.

Kita, N. T., Huss, G. R., Tachibana, S., Amelin, Y., Nyquist, L. E., & Hutcheon, I. D. (2005). *Constraints on the Origin of Chondrules and CAIs from Short-Lived and Long-Lived Radionuclides*. Paper presented at the Chondrites and the Protoplanetary Disk, ASP conference Series, Kaua'i, Hawai'i.

Kleinhans, M. G., Markies, H., de Vet, S. J., in 't Veld, A. C., & Postema, F. N. (2011). Static and dynamic angles of repose in loose granular materials under reduced gravity. *Journal of Geophysical Research*, 116(E11).

Leliwa-Kopystyhski, J., Makkonen, L., Erikoinen, O., & Kossacki, K. J. (1994). Kinetics of pressure-induced effects in water ice/rock granular mixtures and application to the physics of the icy satellites. *Planetary and Space Science*, 42(7), 545-555.

Levison, H. F., Walsh, K. J., Barr, A. C., & Dones, L. (2011). Ridge formation and de-spinning of Iapetus via an impact-generated satellite. *Icarus*, 214(2), 773-778.

Marchi, S., Barbieri, C., Dell'Oro, A., & Paolicchi, P. (2002). Hyperion-Iapetus: Collisional relationships. *Astronomy and Astrophysics*, 381(3), 1059-1065.

Matson, D. L., Castillo-Rogez, J. C., Schubert, G., Sotin, C., & McKinnon, W. B. (2009). The Thermal Evolution and Internal Structure of Saturn's Mid-Sized Icy Satellites. In M. Dougherty, L. Esposito & S. Krimigis (Eds.), *Saturn from Cassini-Huygens* (pp. 577-612): Springer.

Melosh, H. J. (1996). *Impact Cratering: A Geologic Process* (Reprinted ed.). USA: Oxford University Press.

Melosh, H. J., & Nimmo, F. (2009). An intrusive dike origin for Iapetus' enigmatic ridge? Paper presented at the 40th Lunar and Planetary Science Conference, Woodlands, Texas.

Munsell, K. (2012). Cassini Solstice Mission, from <http://saturn.jpl.nasa.gov/index.cfm>

Neukum, G., Wagner, R., Denk, T., Porco, C. C., & Cassini ISS Team. (2005). *The cratering record of the saturnian satellites Phoebe, Tethys, Dione and Iapetus in*

*comparison: First results from analysis of the Cassini ISS imaging data.* Paper presented at the 36th Lunar and Planetary Science Conference.

Owen, T., Cruikshank, D. P., Dalle Ore, C. M., Geballe, T. R., Roush, T. L., de Bergh, C., Meier, R., Pendleton, Y. J., & Khare, B. N. (2001). Decoding the Domino: The Dark Side of Iapetus. *Icarus*, 149(1), 160-172.

Peale, S. J. (1977). Rotation histories of the natural satellites. In J. Burns (Ed.), *Planetary Satellites* (pp. 87-112). Tucson, AZ: Univ. of Arizona Press.

Peale, S. J. (1986). Orbital resonances, unusual configurations, and exotic rotation states among the planetary satellites. In J. A. Burns & M. S. Matthews (Eds.), *Satellites* (pp. 159-224). Tucson, AZ: Univ. of Arizona Press.

Porco, C. C., Baker, E., Barbara, J., Beurle, K., Brahic, A., Burns, J. A., Charnoz, S., Cooper, N., Dawson, D. D., Del Genio, A. D., Denk, T., Dones, L., Dyudina, U., Evans, M. W., Giese, B., Grazier, K., Helfenstein, P., Ingersoll, A. P., Jacobson, R. A., Johnson, T. V., McEwen, A., Murray, C. D., Neukum, G., Owen, W. M., Perry, J., Roatsch, T., Spitale, J., Squyres, S., Thomas, P. C., Tiscareno, M., Turtle, E., Vasavada, A. R., Veverka, J., Wagner, R., & West, R. (2005). Cassini Imaging Science: initial results on Phoebe and Iapetus. *Science*, 307(5713), 1237-1242.

Roatsch, T., Jaumann, R., Stephan, K., & Thomas, P. C. (2009). Cartographic Mapping of the Icy Satellites Using ISS and VIMS Data. *Saturn from Cassini-Huygens* (pp. 763-781). Netherlands: Springer.

Sandwell, D., & Schubert, G. (2010). A contraction model for the flattening and equatorial ridge of Iapetus. *Icarus*, 210(2), 817-822.

Schenk, P., Hamilton, D. P., Johnson, R. E., McKinnon, W. B., Paranicas, C., Schmidt, J., & Showalter, M. R. (2011). Plasma, plumes and rings: Saturn system dynamics as recorded in global color patterns on its midsize icy satellites. *Icarus*, 211(1), 740-757.

Schulson, E. M. (2001). Brittle failure of ice. *Engineering Fracture Mechanics*, 68, 1839-1887.

Singer, K. N., & McKinnon, W. B. (2011). Tectonics on Iapetus: Despinning, respinning, or something completely different? *Icarus*, 216(1), 198-211.

Spencer, J. R., & Denk, T. (2010). Formation of Iapetus' extreme albedo dichotomy by exogenically triggered thermal ice migration. *Science*, 327(5964), 432-435.

Squyres, S. W., & Sagan, C. (1983). Albedo asymmetry of Iapetus. *Nature*, 303, 782-785.

Thomas, P. C. (2010). Sizes, shapes, and derived properties of the saturnian satellites after the Cassini nominal mission. *Icarus*, 208(1), 395-401.

Thomas, P. C., Burns, J., Helfenstein, P., Squyres, S., Veverka, J., Porco, C., Turtle, E., McEwen, A., Denk, T., & Giese, B. (2007). Shapes of the saturnian icy satellites

and their significance. *Icarus*, 190(2), 573-584.

Turcotte, D. L., & Schubert, G. (2002). Elsticity and Flexure. *Geodynamics* (2 ed., pp. 105-131). UK: Cambridge University Press.

USGS Astrogeology. (2009). Gazetteer of Planetary Nomenclature, from <http://planetarynames.wr.usgs.gov/>

van Helden, A. (1984). Saturn through the telescope - A brief historical survey. *Saturn* (pp. 23-43). Tucson, AZ: University of Arizona Press.

Verbiscer, A. J., Skrutskie, M. F., & Hamilton, D. P. (2009). Saturn's largest ring. *Nature*, 461(7267), 1098-1100.

Walcott, R. I. (1970). Flexural Rigidity, Thickness, and Viscosity of Lithosphere. *Journal of Geophysical Research*, 75(20), 3941-&.

Watts, A. B. (2001). Theory of Elastic Plates. *Isostasy and Flexure of the Lithosphere* (pp. 87-112). UK: Cambridge University Press.

Watts, A. B., Karner, G. D., & Steckler, M. S. (1982). Lithospheric Flexure and the Evolution of Sedimentary Basins. *Philosophical Transactions of the Royal Society of London Series a-Mathematical Physical and Engineering Sciences*, 305(1489), 249-281.

Wickert, A. D. (2012). *Lithospheric Flexure and Earth-Surface Processes: 1. Rapid Solutions with Nonuniform Elastic Thickness*.

Willians, D. R. (2012). Planetary Fact Sheet, from <http://nssdc.gsfc.nasa.gov/planetary/factsheet/>

Wilson, P. D., & Sagan, C. (1996). Spectrophotometry and Organic Matter on Iapetus: 2. Models of Interhemispheric Asymmetry. *Icarus*, 122(1), 92-106.

Yeomans, D. K. (2012). Planetary Satellite Physical Parameters, from [http://ssd.jpl.nasa.gov/?sat\\_phys\\_par](http://ssd.jpl.nasa.gov/?sat_phys_par)

Zebker, H. A., Marouf, E. A., & Tyler, L. (1985). Saturn's ring: Particle size distributions for thin layer models. *Icarus*, 64(3), 531-548.